

A UNIFORM ANALYSIS OF THE LY- $\alpha$  FOREST AT  $Z = 0 - 5$ :  
II. MEASURING THE MEAN INTENSITY OF THE EXTRAGALACTIC IONIZING  
BACKGROUND USING THE PROXIMITY EFFECT

JENNIFER SCOTT<sup>1</sup>, JILL BECHTOLD<sup>1</sup>, ADAM DOBRZYCKI<sup>2</sup>, & VARSHA P. KULKARNI<sup>3</sup>

*To appear in the September 2000 Astrophysical Journal Supplement Series*

ABSTRACT

Moderate resolution data for 40 quasi-stellar objects (QSOs) at  $z \approx 2$  were combined with spectra of comparable resolution of 59 QSOs with redshifts greater than 1.7 found in the literature to form a large, homogeneous sample of moderate resolution ( $\sim 1 \text{ \AA}$ ) QSO spectra. These spectra were presented and the statistics of the Lyman  $\alpha$  forest were discussed in Paper I. In this analysis, we demonstrate that a proximity effect is present in the data, ie. there exists a significant ( $5.5\sigma$ ) deficit of lines at  $z_{abs} \approx z_{em}$ . Within  $1.5 h^{-1}$  Mpc of the QSO emission redshift, the significance does depend on QSO luminosity, in accordance with the theory that this effect is caused by enhanced ionization of hydrogen in the vicinity of the QSO from UV photons from the QSO itself. The photoionization model of Bajtlik, Duncan, & Ostriker permits an estimate of the mean intensity of the extragalactic background radiation at the Lyman limit. We compare the results of this standard analysis with those obtained using a maximum likelihood technique. If the spectrum of the background is assumed to be identical to that of each individual QSO, and if this background is assumed to be constant over the redshift range  $1.7 < z < 3.8$ , then the best fit value for  $J(\nu_0)$  is found to be  $1.4^{+1.1}_{-0.5} \times 10^{-21} \text{ ergs s}^{-1} \text{ cm}^{-2} \text{ Hz}^{-1} \text{ sr}^{-1}$ , using QSO redshifts based on the Ly $\alpha$  emission line. Systemic QSO redshifts based on the [OIII]  $\lambda 5007$  emission line for 19 objects in our sample show an average redshift of  $\sim 400 \text{ km s}^{-1}$  with respect to Ly $\alpha$  emission. Using redshifts based on [OIII] or Mg II for the 35 objects for which they are measured and adding  $400 \text{ km s}^{-1}$  to the remaining QSO Ly $\alpha$  redshifts gives a lower value of  $J(\nu_0)$ ,  $7.0^{+3.4}_{-4.4} \times 10^{-22} \text{ ergs s}^{-1} \text{ cm}^{-2} \text{ Hz}^{-1} \text{ sr}^{-1}$ . This value is in reasonable agreement with the predictions of various models of the ionizing background based on the integrated QSO luminosity function. Allowing for the fact that individual QSOs have different spectral indices which may also be different from that of the background, we use the standard methods to solve for the HI photoionization rate,  $\Gamma$ , and the parameters describing its evolution with redshift. The best fit value for the HI ionization rate we derive is  $1.9^{+1.2}_{-1.0} \times 10^{-12} \text{ s}^{-1}$ , in good agreement with models of the background which incorporate QSOs only. Finally, we use simulated Lyman  $\alpha$  forest spectra including the proximity effect to investigate curve-of-growth effects in the photoionization model used in the analysis. We find that the presence of lines on the saturated part of the curve-of-growth could cause our estimates of the background intensity to be overestimated by a factor of two to three. This large absorption line sample and these techniques for measuring the background and understanding the systematics involved allow us to place what we believe are the firmest limits on the background at these redshifts.

*Subject headings:* diffuse radiation — intergalactic medium — quasars: absorption lines

1. INTRODUCTION

The spectra of quasi-stellar objects (QSOs) blueward of Ly $\alpha$  emission show a prodigious number of absorption lines primarily due to Ly $\alpha$  absorption by intervening neutral hydrogen along the line of sight to the QSO (Lynds, 1971; Sargent et al. 1980; Weymann, Carswell, & Smith, 1981). In models of these Ly $\alpha$  systems, they are in photoionization equilibrium with a background ultraviolet radiation field. This radiation field is modeled as the integrated emission from QSOs and young galaxies (Bechtold et al. 1987; Miralda-Escudé & Ostriker 1990; Madau 1992, Meiksin & Madau 1993, Madau & Shull 1996, Haardt & Madau 1996, Fardal et al. 1998).

The basic trend in the number density evolution of Ly $\alpha$  absorbers ( $12 \lesssim \log(N_{HI}) \lesssim 16 \text{ cm}^{-2}$ ) at high redshift in a given QSO spectrum is a steep power law increase with redshift (Sargent et al. 1980). However, a decrease in the number of lines near the emission redshift of an individual QSO relative to the number of lines expected from the power law distribution has been observed (Carswell et al. 1982, Murdoch et al. 1986; Tytler 1987; Bajtlik, Duncan, & Ostriker 1988, hereafter BDO; Lu, Wolfe, & Turnshek 1991, hereafter LWT; Bechtold 1994, hereafter B94). The simplest explanation for this “inverse” effect is enhanced ionization of HI in the vicinity of the QSO by ultraviolet photons from the QSO itself. Thus, the name “proximity

<sup>1</sup>Steward Observatory, University of Arizona, Tucson, AZ 85721, USA,  
e-mail: [jscott,jbechtold]@as.arizona.edu

<sup>2</sup>Harvard-Smithsonian Center for Astrophysics, 60 Garden Street, Cambridge, MA 02138, USA,  
e-mail: adobrzycki@cfa.harvard.edu

<sup>3</sup>Clemson University, Department of Physics and Astronomy, Clemson, SC 29634, USA,  
e-mail: varsha@clemson.edu

effect” is also used. This interpretation, along with the assumptions about the spectrum of the background and the photoionization of the nearby intergalactic medium (IGM) by the QSOs, allows for a measurement of the mean intensity of the ionizing background at the Lyman limit of hydrogen (BDO), which can be compared to estimates of the integrated emission from QSOs.

BDO find that  $J(\nu_0)$  is approximately constant over a redshift range  $1.7 < z < 3.8$ . Expressing  $J(\nu_0)$  as  $J_{-21} \times 10^{-21}$  ergs  $s^{-1}$   $cm^{-2}$   $Hz^{-1}$   $sr^{-1}$ , these authors find  $J_{-21} \approx 1$ . Their best fit form for the dependence of  $J(\nu_0)$  on redshift rules out a luminosity dependent cutoff in the QSO luminosity function (BWLM; Schmidt, Schneider, & Gunn 1986). Several other authors have carried out this analysis on other data sets (LWT, Kulkarni & Fall 1993, hereafter KF93, B94, Williger et al. 1994, Cristiani et al. 1995, Giallongo et al. 1996.) LWT found  $J_{-21} \approx 1$  for  $1.7 < z < 3.8$ ; and B94 found a value consistent with this,  $J_{-21} \approx 3$  for  $1.6 < z < 4.1$ . Srianand & Khare (1996) compile a sample of 69 QSOs from the literature (54 from B94) and obtain  $J_{-21} \approx 6$  for  $1.7 < z < 4.1$ . Williger et al. (1994) find a lower value,  $J_{-21} \approx 0.1 - 0.3$  for  $z \sim 4.2$  from a single  $z=4.5$  QSO; and Giallongo et al. (1996) find  $J_{-21} \approx 0.5$  for  $2.8 < z < 4.1$ , based on high resolution spectra of six QSOs. KF93 re-express the BDO formalism using maximum likelihood techniques and use this to derive  $J(\nu_0) \approx 6 \times 10^{-24}$  ergs  $s^{-1}$   $cm^{-2}$   $Hz^{-1}$   $sr^{-1}$  for  $z \approx 0.5$  from the sample of Bahcall et al. (1993).

In this paper, a homogeneous sample of QSO spectra is used to measure the mean intensity of the ionizing background via the standard proximity effect analysis and the maximum likelihood analysis of KF93. We have presented new Lyman  $\alpha$  forest data for 39 objects with  $1.9 < z_{em} < 2.5$  in Paper I; and supplemented this sample with 59 objects from the literature, and one QSO from the Hamburg/CfA Bright Quasar Survey (Dobrzycki, Engels, & Hagen 1999). The spectra comprising our dataset are of moderate resolution,  $\sim 1 \text{ \AA}$  FWHM; but this is not a disadvantage, as this analysis requires good absorption line statistics and therefore many QSO sight lines. This is difficult to achieve at high resolution, the major reason for using a large set of moderate resolution spectra such as this one.

A major uncertainty in the proximity effect analysis is in the systemic redshifts of the QSOs. Redshifts measured from low ionization permitted lines (e.g. Balmer lines or Mg II) or forbidden lines (e.g. [OIII]  $\lambda\lambda 4959, 5007$ ) lines have been shown to be redshifted with respect to Ly $\alpha$  and C IV emission by up to  $\approx 250 \text{ km s}^{-1}$  (Boroson & Green 1992, Laor et al. 1995). B94 found that increasing the values of the QSO redshifts by  $1000 \text{ km s}^{-1}$  caused the best fit value of  $J_{-21}$  to be decreased by a factor of 3. We therefore obtained emission line spectra for several objects in our sample in order to examine redshift differences between Ly $\alpha$  and [OIII]  $\lambda\lambda 4959, 5007$ , Mg II or Balmer emission. We investigate the effect of these shifts on the value of  $J(\nu_0)$  derived.

In Section 2 the spectra used to measure Lyman limit fluxes for some of our sample objects and spectra used to perform systemic redshift measurements of several QSOs in our sample are presented. In Section 3 the techniques used to measure the mean intensity of the HI ionizing back-

ground at the Lyman limit are discussed, which includes discussions of the QSO systemic redshifts in Section 3.5 and the HI ionization rate measurements in Section 3.6. In Section 4 we present Lyman  $\alpha$  forest simulations and investigate curve-of-growth effects in the proximity effect analysis. Section 5 is a summary and discussion of our results and the possible systematic effects entering into our analysis.

Throughout this paper, we assume values of  $75 \text{ km s}^{-1} \text{ Mpc}^{-1}$  for  $H_0$  and 0.5 for  $q_0$ .

## 2. DATA

### 2.1. Spectrophotometry

Spectrophotometry of 12 sample objects in the spectral region between Ly $\alpha$  and C IV emission was obtained at the Steward Observatory (SO) Bok Telescope with the Boller and Chivens (B&C) Spectrograph and the  $1200 \times 800$  CCD on the nights of September 22, 1992, November 29, 1994, and March 28, 1995. Observations were made with a  $400 \text{ l mm}^{-1}$  grating with  $\lambda_b=4889 \text{ \AA}$  in the first order and a  $4.5''$  slit. Spectrophotometry of the object 1422+231 was obtained at the SO B&C using a  $600 \text{ l mm}^{-1}$  grating with  $\lambda_b=6681 \text{ \AA}$  in the first order and a  $1.5''$  slit on April 22, 1996; and the object 1603+383 was observed by A.D. as part of the Hamburg/CfA Bright Quasar Survey on July 4, 1995 with the Fred Lawrence Whipple Observatory 1.5-meter Tillinghast telescope and FAST spectrograph, using a  $300 \text{ l mm}^{-1}$  grating with  $\lambda_b=4750$  in the first order and a  $3''$  slit. See Table 1 for a summary.

All observations except those of 1422+231 and 1603+383 were made with the slit set at the parallactic angle. This should not seriously effect the spectrophotometry of 1603+383 as it was observed at a small airmass. Additionally, however, the observation of 1422+231 was made with a slit width that is somewhat small for optimal spectrophotometry. In any case, as discussed further below, both 1422+231 and 1603+383 are excluded from the proximity effect analysis due to the fact that 1422+231 is a gravitational lens and the presence of associated absorption in the spectrum of 1603+383. Any small errors in the spectrophotometry of the 74 objects used in the proximity effect analysis should not significantly bias the results of this work.

Object spectra were bias corrected and extracted using standard IRAF packages using He-Ne-Ar and quartz calibration exposures taken at each telescope position to perform the wavelength calibration and to correct for pixel-to-pixel variations, respectively. The data were then flux calibrated using standard star exposures. The column density of Galactic neutral hydrogen along the line of sight to each object was found using the program COLDEN, made available by J. M<sup>c</sup>Dowell; and the spectra were corrected for the Galactic reddening calculated from the relation  $N_{HI}/E(B - V) = 4.8 \times 10^{21} \text{ atoms cm}^{-2} \text{ magnitude}^{-1}$  (Bohlin et al. 1978). The spectra and the power law continuum fits are shown in Figure 1.

### 2.2. QSO Systemic Redshifts

For the present absorption line sample, the QSO narrow emission lines discussed above all lie redward of  $\sim 7600 \text{ \AA}$ , and into the near infrared. Spectra of four objects in this sample were obtained at the MMT with the infrared spec-

trometer FSpec (Williams et al. 1993) on May 20, 1994 (1207+399 and 1422+231) and April 1, 1996 (1408+009, and 1435+638) using a  $75 \text{ l mm}^{-1}$  grating and a  $1.2''$  slit giving a resolution of  $\sim 34 \text{ \AA}$  in the K band. A series of exposures of each object was taken. Between each exposure, the object was moved along the slit. The total integration time is listed in Table 2. One object, 0836+710, was observed on March 28, 1995 with the B&C, the  $1200 \times 800$  CCD, a  $300 \text{ l mm}^{-1}$  grating with  $\lambda_b = 6693 \text{ \AA}$  in the first order, and a  $4.5''$  slit. Infrared spectra of eight objects in this sample, 0000-263, 0014+813, 0636+680, 0956+122, 1159+124, 1208+101, 2126-158, were obtained using FSpec, OSIRIS on the Cerro Tololo Inter-American Observatory 4 m telescope, and CRSP on the Kitt Peak National Observatory 4 m telescope (Kuhn 1996). A summary of these observations is given in Table 2 and the spectra are displayed in Figure 2.

### 3. $\text{Ly}\alpha$ FOREST STATISTICS FOR $Z_{ABS} \approx Z_{EM}$ : THE PROXIMITY EFFECT

#### 3.1. Spectrophotometry

In order to perform the proximity effect analysis, the flux of each QSO at the Lyman limit is needed. The spectrophotometry data discussed above was used for this purpose. A power law of the form  $f_\nu \sim \nu^{-\alpha}$  was fit to the continua of these objects. The straight line fit to  $\log(f_\nu)$  vs.  $\log(\nu)$  was done using a robust estimation technique; and emission lines found by visually inspecting the spectrum were excluded from the points used in the fit. The measured flux at  $1450 \text{ \AA}$  and the value of  $\alpha$  derived from this fit were used to determine the flux at  $912 \text{ \AA}$ . For the objects we did not observe, we proceed as follows. If a flux measurement at a rest UV wavelength other than  $912 \text{ \AA}$  exists along with a published spectral index, we use these to extrapolate to the Lyman limit. If no spectral index is available, we use the value of 0.46 (Francis 1996). The object 2134+004 has a variable continuum (Perez et al. 1989, Corbin 1992). Therefore, although we have spectrophotometry from our own observations of this object, we take the flux measurement of these authors from their averaged spectrum produced from observations made over several months. We use this with the spectral index we derive to extrapolate to  $912 \text{ \AA}$ .

If no rest UV spectrophotometry of an object exists, we estimate  $f_\nu$  at  $5500 \text{ \AA}$  (observed) from the V magnitude given in Table 1 of Paper I with an extinction correction applied. The extinction correction was calculated using the column density of neutral hydrogen from COLDEN and the Seaton (1979) re-normalization of the composite UV-optical reddening curve of Nandy et al. (1975, and references therein). A rest-frame composite QSO spectrum (Zheng et al. 1997) with an arbitrary flux scale was redshifted by the appropriate amount for each object. The flux in the V filter was calculated by convolving this spectrum with the V filter transmission as a function of wavelength. A scaling factor was calculated so that when the redshifted QSO composite spectrum was multiplied by this factor, the resulting magnitude matched the magnitude listed in Table 1 of Paper I. The flux at  $1450 \text{ \AA}$  was then taken from this scaled spectrum and this flux was extrapolated to the Lyman limit using the spectral index given in Table 3. A zero point flux density for the V filter

of  $3.81 \times 10^{-20} \text{ ergs s}^{-1} \text{ cm}^{-2} \text{ Hz}^{-1}$  (Johnson 1966) was used.

The asterisks in Table 3 mark QSOs which are known lenses or which show associated absorption in their spectra. Associated absorption is defined to be any Lyman  $\alpha$  absorption within  $\sim 5000 \text{ km s}^{-1}$  of the QSO redshift which also shows metal lines. (See Paper I for a description of the metal line systems identified in each QSO spectrum.) These objects were excluded from the proximity effect analysis on the grounds that gas associated with the QSO or QSO host galaxy is not part of the general intergalactic medium and bulk motions within this gas may skew the results. The spectrophotometric properties adopted for the 59 QSOs from the literature are listed in Table 5 of B94.

#### 3.2. Number of Lines with $z_{abs} \approx z_{em}$

The first method we use to demonstrate the proximity effect is to compare the number of lines predicted if there was no effect from the equation

$$\frac{d\mathcal{N}}{dz} = \mathcal{A}_0(1+z)^\gamma. \quad (1)$$

with the number of lines counted in the spectrum as a function of distance from the QSO,

$$\Delta\mathcal{N} = \mathcal{N}_{pred} - \mathcal{N}_{obs}. \quad (2)$$

The number of lines predicted is found by integrating Equ. 1,

$$\mathcal{N}_{pred} = \frac{\mathcal{A}_0}{\gamma+1} ((1+z_{max})^{\gamma+1} - (1+z_{min})^{\gamma+1}). \quad (3)$$

The bins in luminosity distance from the QSO are defined according to the relation,

$$\Delta R = 1687.5 \frac{\Delta z}{(1+z_{em})^{5/2}} h^{-1} \text{ Mpc}. \quad (4)$$

We use  $h = 0.75$ . Figure 3 plots the distribution in  $z$  and Lyman limit luminosity of the QSOs in our sample.

The dataset was divided into low luminosity and high luminosity subsamples at  $\log[L(\nu_0)] = 31.1$ , such that there were equal numbers of objects in each subsample. The Lyman limit luminosity of each object was calculated according to the expression

$$L(\nu_0) = 4\pi d_L^2 \frac{f(\nu_0)}{(1+z_{em})} \quad (5)$$

where the luminosity distance to the QSO,  $d_L$  is given by

$$d_L = \frac{c\{q_0 z + (q_0 - 1)[(1 + 2q_0 z)^{1/2} - 1]\}}{q_0^2 H_0} \quad (6)$$

for  $q_0 > 0$ . In this paper, we use a value of 0.5 for  $q_0$ . Figure 4 plots the fractional deficit of lines,  $(\mathcal{N}_{pred} - \mathcal{N}_{obs})/\mathcal{N}_{pred}$ , for the total sample and the high and low luminosity subsamples.

For the total sample, a  $5.5\sigma$  deficit of lines is found in the  $0.1\text{-}1.5 h^{-1} \text{ Mpc}$  bin. The low luminosity subsample shows a deficit of lower significance ( $3.6\sigma$ ) than the high luminosity subsample ( $4.6\sigma$ ). These deficits are expected for a proximity effect caused by enhanced ionization of HI from the QSO flux; and the marginally higher significance for high luminosity objects further suggests that this picture is legitimate.

### 3.3. Photoionization Model

We follow the formalism outlined in BDO to calculate a value of the mean intensity of the ionizing background in the redshift range  $1.7 < z < 3.4$ . The column density of a Ly $\alpha$  absorber in the immediate vicinity of a QSO will be modified from the value that it would have if the QSO were not present. The amount by which the column density of HI will be reduced due to ionization by UV photons from the QSO is given by

$$N = N_0(1 + \omega)^{-1} \quad (7)$$

where  $N$  is the observed column density of the absorber, and  $N_0$  is the column density that the absorber would have if the QSO were absent. The column density distribution of the general Ly $\alpha$  absorber population was shown to follow a power law over several orders of magnitude in column density,

$$\mathcal{N} \propto N^{-\beta}, \quad (8)$$

which, for a fixed limiting column density,  $N_{thr}$ , (corresponding to the limiting rest equivalent width) can be integrated to give the total number of lines with column densities equal to or larger than the limiting value,  $\mathcal{N}(N \geq N_{thr}) = N_{thr}^{-(\beta-1)}$ . Thus, a proximity effect-corrected redshift distribution for a fixed rest equivalent width threshold can be derived:

$$\frac{d\mathcal{N}}{dz} = \mathcal{A}_0(1+z)^\gamma [1 + \omega(z)]^{-(\beta-1)} \quad (9)$$

where  $\omega$  represents a flux-scaled distance of each cloud from the QSO

$$\omega = \frac{F^Q(\nu_0)}{4\pi J(\nu_0)}. \quad (10)$$

Here,  $F^Q(\nu_0)$  is the Lyman limit flux density due to the QSO at the position of a given absorber,

$$F^Q(\nu_0) = \frac{L(\nu_0)}{4\pi r_L^2} \quad (11)$$

where  $r_L$  is the luminosity distance between the QSO and the absorber. We remove the dominant dependence of the line density on redshift by introducing a coevolving coordinate,  $X_\gamma$ , given by

$$X_\gamma = \int (1+z)^\gamma dz. \quad (12)$$

If no proximity effect existed, the number of lines per coevolving coordinate would be expressed as

$$d\mathcal{N}/dX_\gamma = \mathcal{A}_0. \quad (13)$$

In this analysis, we use a value for  $\beta$  of 1.46 from Hu et al. (1995) based upon high S/N, high resolution spectra of four QSOs at  $z \approx 3$ , consistent with the value of 1.4 found by Dobrzycki & Bechtold (1996), hereafter DB96, from simulations of Ly $\alpha$  forest spectra in QSOs at  $z \approx 3$ . The value of this parameter is an important factor in the ionization model. B94 found that changing the adopted value of  $\beta$  from 1.7 to 1.4 caused the derived value of  $J_{-21}$  to decrease by a factor of  $\sim 3$ . Giallongo et al. (1996) find

that a double power law provides a better fit to the observed column density distribution in their high resolution spectra than a single power law. The form of their double power law consists of a break at  $N_{HI} = 10^{14} \text{ cm}^{-2}$  and values of  $\beta$  above and below this break of 1.8 and 1.4 respectively. For this analysis, however, we will use a single power law, as the data of Hu et al. (1995) do not require the double power law form.

The procedure consists of assuming a form for  $J(\nu_0)$  as a function of  $z$ , dividing the lines into the appropriate  $\omega$  bins, and finding the parameters of the assumed form of  $J(\nu_0)$  that gives the lowest  $\chi^2$  between the binned data and the ionization model. Since no work to date has shown that  $J(\nu_0)$  evolves significantly with redshift over the range of our sample objects, we will treat the case that  $J(\nu_0)$  is constant over the redshift range of the data.

Figure 5 plots  $\chi^2$  with respect to the constant  $J(\nu_0)$  photoionization model versus  $\log[J(\nu_0)]$  and Figure 6 plots the coevolving number density versus  $\omega$  for the lowest  $\chi^2$  value of  $J(\nu_0)$  for each subsample. The results of this analysis are summarized in Table 4 and are discussed in more detail in Section 5.

### 3.4. Maximum Likelihood Analysis

In addition to the standard BDO analysis, we also used a maximum likelihood method outlined by KF93 to measure the extragalactic ionizing background in a manner that avoids binning of the data. One constructs a likelihood function of the form

$$L = \prod_a f(N_a, z_a) \prod_Q \exp\left[-\int_{z_{min}^Q}^{z_{max}^Q} dz \int_{N_{min}^Q}^{\infty} f(N, z) dN\right], \quad (14)$$

where the subscripts  $a$  and  $Q$  refer to absorbers and QSOs and where  $f(N, z)$  is the standard equation for the distribution of Lyman  $\alpha$  absorbers in column density and redshift,

$$f(N, z) = AN^{-\beta}(1+z)^\gamma [1 + \omega(z)]^{-(\beta-1)}. \quad (15)$$

The parameter  $\omega$  is defined as above, but here, the normalization in terms of  $\mathcal{A}_0$  in Equation 1 is given by  $\mathcal{A}_0(N_{lim}/N_0)^{\beta-1}(\beta-1)^{-1}$ . With the exception of the case in which a variable threshold is used,  $N_{min}$  for each QSO is the column density which, according to the curve-of-growth adopted (see KF93), corresponds to an equivalent width of  $0.32 \text{ \AA}$ ,  $2.62 \times 10^{14} \text{ cm}^{-2}$ .

Instead of using the method outlined by KF93 whereby the parameters  $A, \beta, \gamma$ , and  $J(\nu_0)$  are all found by minimizing  $-\ln(L)$  where  $L$  is given by the likelihood function above, we chose to take the parameter  $\gamma$  from a separate maximum likelihood solution to Equation 1 (see Paper I.) Since our spectra are more highly blended than the low redshift data used by KF93, we choose not to determine  $\beta$  directly from our data using line equivalent widths and the curve-of-growth and instead adopt a value found from high resolution spectra. As described in the previous section, we take  $\beta$  to be 1.46 (Hu et al. (1995) and solve for  $A$  by requiring  $f(N, z)$  to give the observed number of lines in the regions of the QSO spectra unaffected by the proximity effect.

We ran two tests on this set of algorithms. The first of these was to attempt to reproduce the results of KF93 with

the dataset they used from Bahcall et al. (1993). Next, we used a high redshift subsample of our complete dataset, the DB96 sample, to compare the results of the maximum likelihood analysis and the BDO analysis to each other and to independent checks on these values (B94, Giallongo et al. 1996).

We were able to reproduce the results of KF93. Using their Sample 2, the Bahcall et al. (1993) sample minus one BAL QSO, PG 0043+039, we obtain  $(\gamma, \beta, \log(A)) = (0.23, 1.47, 7.74)$  and  $\log[J(\nu_0)] = -23.0_{-0.6}^{+0.7}$  for  $b = 35 \text{ km s}^{-1}$ . These agree with the values they find,  $(\gamma, \beta, \log(A)) = (0.21, 1.48, 7.74)$ , and the errors in these values,  $\sigma_\gamma \sim 0.06$ ,  $\sigma_\beta \sim 0.05$ , and  $\sigma_{\log(A)} \sim 0.1$ . Their result for  $\log[J(\nu_0)]$  for this sample is  $-23.3_{-0.5}^{+0.7}$ .

The high redshift subsample we created consisted of 518 lines from the 15 objects from DB96 that do not show associated absorption. The QSOs have redshifts between 2.52 and 3.38. Using our maximum likelihood program to solve for the Ly $\alpha$  forest statistics, we find  $\gamma = 1.926 \pm 0.656$ , and  $\log(A) = 7.03$  for  $N_{min} = 2.6 \times 10^{14} \text{ cm}^{-2}$  and  $\beta = 1.46$ . This subsample does give similar results in the BDO and the maximum likelihood cases,  $\log[J(\nu_0)] = -21.40_{-0.69}^{+1.10}$  and  $\log[J(\nu_0)] = -21.58_{-0.23}^{+0.30}$ , respectively. (See rows 1 and 2 of Table 4.) These values agree well with the Giallongo et al. (1996) result of  $\log[J(\nu_0)] = -21.30 \pm 0.7$  for  $z = 1.7-4.1$ .

The software we used for the maximum likelihood analysis uses all regions of the QSO spectra between  $z_{min}$ , specified by the spectral coverage or by Ly $\beta$  emission, and  $z_{max}$ , specified by Ly $\alpha$  emission. Though it does not count lines associated with identified metal line systems, it does not exclude the regions of the spectrum where these lines lie. To ensure that this does not have a significant effect on our resultant solution for the background, we tested a program that does exclude regions of the spectra in the same way that our BDO-style software does. The change in the result was indeed insignificant; but taking these excluded spectral regions into account and binning the data in the same way the BDO-style software does brings the maximum likelihood and the BDO method results into excellent agreement.

Figure 7 plots the log of the ratio of the likelihood function to the maximum value versus  $\log[J(\nu_0)]$ ; and Figure 8 plots the coevolving number distribution of Ly $\alpha$  lines with respect to  $\omega$  just as in Figure 6. The results of this analysis are also summarized in Table 4 and discussed further in Section 5.

### 3.5. Systemic QSO Redshifts

One of the major uncertainties in the proximity effect analysis is in the systemic redshifts of the QSOs. If the true redshift of a QSO is higher than the value used in the analysis, any given cloud is further away from the QSO than assumed. Hence, the influence of the QSO at this cloud is less than inferred and the value of  $J(\nu_0)$  in reality is lower than the one derived.

For the data presented in Figure 2, an average of several cursor settings at the peak of the emission line was used to determine the line centers. More detailed fits were not done as our purpose lies mainly in determining if any gross shifts between Ly $\alpha$  and the Balmer lines/[OIII]/Mg II exist for our data; but we found no significant difference

between this method and making Gaussian fits to the upper 50% of the emission line profiles.

Ly $\alpha$  redshifts were measured from the absorption line spectra when the entire Ly $\alpha$  profile was observed, in the same way as was done for the Balmer, [OIII], and Mg II lines. Table 5 lists the adopted best redshift value for each emission line for each object supplementing our measurements with measurements from the literature.

Laor et al. (1994) and Laor et al. (1995) found, from a sample of 13 QSO spectra from the Faint Object Spectrograph on Hubble Space Telescope between redshifts of  $z \sim 0.16$  and  $z \sim 2.0$ , average velocity shifts between [OIII]  $\lambda 5007$  and Ly $\alpha$ , Mg II, and H $\beta$  of  $200 \pm 150 \text{ km s}^{-1}$ ,  $-85 \pm 130 \text{ km s}^{-1}$ , and  $-75 \pm 110 \text{ km s}^{-1}$ , respectively. This agrees with the Corbin & Boroson (1996) result for 48 objects with  $0.03 < z < 0.77$ . They found mean [OIII]-Ly $\alpha$  and [OIII]-H $\beta$  shifts of  $191 \pm 101 \text{ km s}^{-1}$  and  $-75 \pm 57 \text{ km s}^{-1}$ . Thus, Ly $\alpha$  is blueshifted with respect to [OIII] by  $\sim 200 \text{ km s}^{-1}$ , while Mg II and H $\beta$  are marginally redshifted with respect to [OIII]. Tytler & Fan (1992) find a mean [OIII]-H $\beta$  shift of  $-15 \pm 37 \text{ km s}^{-1}$  from 8 QSOs with redshifts between  $\sim 0.3$  and  $\sim 0.6$  and conclude that both Balmer lines and narrow forbidden lines give redshifts within  $100 \text{ km s}^{-1}$  or less of the QSO systemic redshift. They then find a blueshift of Mg II with respect to [OIII]/H $\beta$  for 100 QSOs of  $101 \pm 47 \text{ km s}^{-1}$  which they use as a secondary systemic redshift zero point in their analysis of a large QSO sample. The magnitude of the blueshift of Ly $\alpha$  with respect to [OIII]/H $\beta$  that they derive is  $172 \pm 17 \text{ km s}^{-1}$ . The data of Nishihara et al. (1997) for five QSOs at  $z \sim 1.5$  show a negligible redshift of Mg II with respect to [OIII],  $31 \pm 411 \text{ km s}^{-1}$ . However these five objects show a somewhat larger redshift of H $\beta$  with respect to [OIII]  $\lambda 5007$ , equalling  $260 \pm 522 \text{ km s}^{-1}$ , consistent with the fact that these objects have high luminosities. M<sup>c</sup>Intosh et al. (1999b) use the near-infrared spectra of QSOs at  $2.0 \lesssim z \lesssim 2.5$  presented in M<sup>c</sup>Intosh et al. (1999a) to examine the redshift differences between [OIII] and H $\beta$ . They supplement their data with data from the literature to measure the redshift differences between [OIII] and Mg II. They find that on average, H $\beta$  is redshifted relative to [OIII] by  $520 \pm 80 \text{ km s}^{-1}$  for 21 of their sample objects, while Mg II lies within  $50 \text{ km s}^{-1}$  of the redshift of [OIII] for 12 sample objects.

For our sample, we find that Ly $\alpha$  is blueshifted with respect to [OIII]  $\lambda 5007$  by  $382 \pm 1160 \text{ km s}^{-1}$  for 19 QSOs. Mg II emission is blueshifted by an average of  $338 \pm 901 \text{ km s}^{-1}$  with respect to [OIII] on the basis of seven measurements. We find that H $\beta$  is redshifted by  $642 \pm 740 \text{ km s}^{-1}$  with respect to [OIII] on the basis of five measurements. Including three H $\alpha$  redshifts listed in Table 5 with these H $\beta$  redshifts leads to a  $507 \pm 615 \text{ km s}^{-1}$  redshift of Balmer lines with respect to [OIII]. This shift is larger than that discussed above for low redshift QSOs. However, it is consistent with the Nishihara et al. (1997) H $\beta$  shift for high luminosity QSOs. Combining our data with that of these authors, we find that Mg II is blueshifted with respect to [OIII] by  $184 \pm 735 \text{ km s}^{-1}$ . Including the data of M<sup>c</sup>Intosh et al. (1999b) that is not already in our sample gives a blueshift of  $95 \pm 603 \text{ km s}^{-1}$ . Similarly, combining our data with that of Nishihara et al. (1997), we find that H $\beta$  is redshifted with respect to [OIII] by  $451 \pm 636$

km s<sup>-1</sup>. After supplementing this combined data set with the data of M<sup>c</sup>Intosh et al. (1999b), the redshift becomes 379 ± 516 km s<sup>-1</sup>. Finally, combining the data of M<sup>c</sup>Intosh et al. (1999b) with ours gives a Ly $\alpha$  blueshift of 418 ± 920 km s<sup>-1</sup> with respect to [OIII].

As has been noted in previous work, the standard error in the mean velocity shifts is quite large, on the order of or exceeding the value of the shift itself. We estimate that the wavelength calibration errors in our data contribute a  $\sim 10$ -30 km s<sup>-1</sup> error in the derived redshifts; and the spread in different redshift measurements of the same species (e.g. Balmer lines or [OIII]  $\lambda 4959$  and  $\lambda 5007$ ) for the same object is typically 100-200 km s<sup>-1</sup>. The observed spreads in the velocity differences of the Ly $\alpha$ , Mg II, and Balmer emission lines with respect to the QSO systemic redshifts are much larger than this, indicating that it is intrinsic to the QSO population. Figure 9 shows histograms of the emission line redshift differences between [OIII] and Ly $\alpha$ , [OIII] and Mg II, and [OIII] and Balmer lines. Our results are plotted with those of Laor et al. (1995) and of Nishihara et al. (1997). Our sample shows no well-defined mean [OIII]-Balmer shift, just a large scatter in the measurements included. Our sample also shows a large range of [OIII]-Ly $\alpha$  and [OIII]-Mg II shifts with no well-defined mean value. Nonetheless, the mean trend is that the [OIII]-Ly $\alpha$  shift is different from zero by 1.4 $\sigma$  for our data, less than the 3.5 $\sigma$  significance found by Laor et al. (1995). The [OIII]-Balmer line shifts for both our data set and for our data combined with that of Nishihara et al. (1997) are *more* significant, 2.7 $\sigma$  and 2.8 $\sigma$  respectively. The [OIII]-Mg II shift is consistent with zero in a mean sense, but with large scatter. Thus, though better statistics are desirable, it seems that for these high redshift and relatively high luminosity objects, Balmer lines are not good indicators of the QSO systemic redshift. For the purposes of this study therefore, we treat only the redshifts found from [OIII]  $\lambda 5007$  for 19 objects in our sample and Mg II for 16 objects in our sample as systemic QSO redshifts.

### 3.6. The HI Ionization Rate

The HI ionization rate due to a source of UV flux is formally given by the equation:

$$\Gamma = \int_{\nu_0}^{\infty} \frac{4\pi J(\nu)\sigma_{HI}(\nu)}{h\nu} d\nu \text{ s}^{-1}. \quad (16)$$

The calculations of the mean intensity of the ionizing background to date have made a critical assumption, namely that the spectrum of the background and the spectra of the individual QSOs are identical. This allows the expression  $\omega = \Gamma^Q/\Gamma^{bg}$  to reduce to the ratio of the Lyman limit flux density of the QSO,  $J^Q(\nu_0)$ , to that of the background,  $J^{bg}(\nu_0)$ , for each line (BDO). Since the IGM reprocesses the radiation emitted from QSOs, this is not strictly true (Miralda-Escudé & Ostriker 1990, Madau 1991, 1992, Meiksin & Madau 1993, Haardt & Madau 1996, Fardal et al. 1998). Furthermore, the value of  $\Gamma^{bg}$  is of particular interest as it can be used to infer the value of  $\Omega_b$  by comparing the distribution of flux decrements in high resolution QSO spectra to Lyman  $\alpha$  forest simulations (Rauch et al. 1997). Therefore, we repeat the standard BDO analysis without making this assumption,

ie. using  $\omega = \Gamma^Q/\Gamma^{bg}$  and solving for the HI ionization rate from the metagalactic background radiation. The ionization rate for each QSO was calculated using Equation 16, where  $\sigma_{HI}(\nu) = 6.3 \times 10^{-18} (\frac{\nu_0}{\nu})^3 \text{ cm}^2$  and where  $J^Q(\nu) = J^Q(\nu_0)(\frac{\nu}{\nu_0})^{-\alpha}$ . For each QSO,  $J^Q(\nu_0)$  is the same value used in the standard analysis used to solve for  $J^{bg}(\nu_0)$ , and  $\alpha$  is given in Table 3. For some objects, no  $\alpha$  listed in this table and a value of 0.46 was used, as described in Section 3.1. As before, the best value will be the one that gives the lowest  $\chi^2$  between the model with  $\beta=1.46$  and the binned data. We use the narrow line redshifts for each QSO discussed above and add 400 km s<sup>-1</sup> to each QSO redshift measured from the Lyman  $\alpha$  emission line.

Haardt & Madau (1996) present a Gaussian fit to their model for the evolution of  $\Gamma$  with redshift,

$$\Gamma = A(1+z)^B \exp[-(z-z_c)^2/S] \quad (17)$$

that agrees with their detailed model for the background to within 10% over the range  $0 < z < 5$ . The best fit parameters they derive for  $q_0=0.5$  are  $A=6.7 \times 10^{-13} \text{ s}^{-1}$ ,  $B=0.43$ ,  $z_c=2.30$ , and  $S=1.95$ . Fardal et al. (1998) fit their model for the background with the parameter sets  $A=5.6 \times 10^{-13} \text{ s}^{-1}$ ,  $B=0.60$ ,  $z_c=2.22$ , and  $S=1.90$  and  $A=1.26 \times 10^{-12} \text{ s}^{-1}$ ,  $B=0.58$ ,  $z_c=2.77$ , and  $S=2.38$  for the Q1 and Q2 luminosity functions, of Pei (1995) respectively. Incorporating this expression for  $\Gamma(z)$  with these three different sets of parameters into the BDO style analysis allows us to determine which of these models fits our data best. The results are listed in Table 6 and are discussed in greater depth below in Section 5.

## 4. SIMULATIONS AND THE CURVE OF GROWTH

Simulated Lyman  $\alpha$  forest spectra for the DB96 sample only were produced using the software described in that paper. The simulation input  $\gamma$  was changed slightly to reflect the maximum likelihood value found by the software used in the analysis described in Paper I. The normalization was chosen to give matching amounts of total absorption in the real and simulated spectra. The parameters used were  $\gamma = 2.069$ ,  $\mathcal{A}_0 = 4.835$ ,  $\beta = 1.46$ ,  $\log(N_{\text{HI,min}}) = 13.0$ ,  $\log(N_{\text{HI,max}}) = 16.0$ ,  $\langle b \rangle = 28.0 \text{ km s}^{-1}$ ,  $\sigma_b = 10.0 \text{ km s}^{-1}$ , and  $b_{\text{cut}} = 20.0 \text{ km s}^{-1}$ .

The proximity effect was included in these simulations by simply modifying each cloud's column density according to equations 7 and 10. The value of  $\log[J(\nu_0)]$  from the BDO type analysis on the DB96 sample is  $-21.40_{-0.69}^{+1.1}$ . Values of -19.0, -20.0, -21.3, -22.0, and -23.0 for  $\log[J(\nu_0)]$  were input and the analyses described above were used to recover that  $J(\nu_0)$ . Two examples of the simulated spectra are shown in Figure 10.

The analysis considers all lines above a fixed equivalent width threshold of 0.32 Å. Thus, as the column densities of lines are modified by the QSO flux from their expected values in the absence of the proximity effect, the equivalent widths of the lines will change according to the curve-of-growth. If a line is saturated, changing its column density will have little effect on its equivalent width, since it lies on the flat part of the curve-of-growth where  $W \propto \sqrt{\log(N)}$ . This will mean that for a given equivalent width cutoff in the data, this line will not drop out of the sample as the proximity effect is turned on in the simulations. Since the

line deficit will be less than expected for a given input value of  $J(\nu_0)$ , the proximity effect will appear less pronounced and the true  $J(\nu_0)$  will be overestimated. We found this to be the case from our simulations. As Figure 11 illustrates and Table 7 summarizes, though the values of  $J(\nu_0)$  recovered from the simulated data were usually consistent with the input values within the  $1\sigma$  confidence limits, they were systematically larger than the input values by up to a factor of 3. The largest input values of  $\log[J(\nu_0)]$ , -19.0 and -20.0, give the largest discrepancy between this input value and the  $\log[J(\nu_0)]$  recovered from the BDO analysis performed on the simulated spectra. The smallest input value of  $\log[J(\nu_0)]$ , -23.0, gives the smallest discrepancy between the input and recovered values. However, the  $1\sigma$  confidence limits on this fit are also relatively small, making it the only trial which does not recover the input  $\log[J(\nu_0)]$  to within those limits.

To demonstrate the effect, Figure 12 compares the simulated line equivalent widths with and without the proximity effect included. The column density of each line from the simulated spectra line lists with no proximity effect were modified according to equations 7 and 10. Figures 12(a-e) plot the nonproximity effect rest equivalent width  $W_{no-PE}$  versus the ratio of the proximity effect and nonproximity effect equivalent widths,  $W_{PE}/W_{no-PE}$ . The solid line delineates the detection threshold for the lines in the list for which the proximity effect is included,  $W_{PE}=0.32 \text{ \AA}$ . Absorption lines that fall above this line were not removed from the sample when the proximity effect was turned on, while those below it disappeared. For a given set of QSOs with fixed Lyman limit luminosities, such as this one, the proximity effect signature in their spectra will become less pronounced as the ambient UV background increases. Therefore, as  $\log[J(\nu_0)]$  increases from -23.0 to -19.0, the magnitude of the proximity effect decreases, and the proximity effect line list differs less and less from the nonproximity effect line list.

## 5. RESULTS AND DISCUSSION

Table 4 lists the best fit values of  $J(\nu_0)$  found for various subsamples of this dataset using both the canonical BDO and the maximum likelihood methods. For the BDO method, the  $1\sigma$  confidence limits are found from a  $\Delta\chi^2$  of 8.18 for 7 degrees of freedom. The maximum likelihood method  $1\sigma$  confidence limits derive from the fact that  $\ln(L/L_{max})$  is distributed as  $\chi^2/2$ . The total sample consisting of 74 QSOs with all QSO redshifts based on the Ly $\alpha$  emission line gives a best fit value of  $\log[J(\nu_0)]$  of  $-20.90^{+0.61}_{-0.48}$  for the BDO analysis and  $-20.83^{+0.23}_{-0.20}$  for the maximum likelihood analysis.

As the results in Table 4 demonstrate, using narrow line redshifts for 35 of the 74 QSOs for which they have been directly measured and Ly $\alpha$  redshifts for the rest does not change the result. However, when  $400 \text{ km s}^{-1}$  is added to the Ly $\alpha$  redshifts of the objects with no measured narrow line redshift, a value for  $\log[J(\nu_0)]$  of  $-21.15^{+0.17}_{-0.43}$  is derived using the BDO method and  $\log[J(\nu_0)]=-21.17^{+0.19}_{-0.15}$  is found using the maximum likelihood method. Recall that the mean blueshift of Ly $\alpha$  with respect to [OIII] for the 19 objects in this paper with [OIII]  $\lambda 5007$  measurements was found to be  $\sim 400 \text{ km s}^{-1}$ . This decrease in the mean intensity of the background derived when larger

QSO redshifts are used is to be expected. (cf. Section 3.5) Because this measurement of the background accounts for the systematic blueshift of the Ly $\alpha$  emission line with respect to the systemic redshift of each QSO, we consider it to be our best estimate for the mean intensity of the background at the Lyman limit.

These measurements have been made, however, using a photoionization model with somewhat unrealistic assumptions, particularly that Ly $\alpha$  absorbers are isothermal and are composed of pure hydrogen. For clouds with a primordial He abundance and which are in thermal and ionization equilibrium, Using CLOUDY to model the ionization state of absorbers with a metal abundance of  $10^{-2}$  solar (Cowie et al. 1995, Tytler & Fan 1994) as a function of  $\omega$ , we find that the neutral fraction,  $\chi$ , is proportional to  $(1+\omega)^{-1.21}$ . This implies that

$$\frac{dN}{dz} = \mathcal{A}_0(1+z)^\gamma [1+\omega(z)]^{-1.21(\beta-1)} \quad (18)$$

In this scenario, the optimal value found for  $\log[J(\nu_0)]$  is  $-21.10^{+0.53}_{-0.28}$ . This value is marginally larger than the value discussed above, found under the assumption of absorbers composed of pure hydrogen; but it is not significantly different, so we conclude that the absence of metals in the BDO model has not drastically affected our measurement of the background.

It is worth noting that 16 objects in our sample of objects with no associated absorption show evidence for damped Ly $\alpha$  absorption: 0058+019, 0100+130, 0334-204, 0913+072, 0938+119, 0952+338, 0955+472, 1009+299, 1017+280, 1215+333, 1247+267, 1548+092, 1946+770, 2126-158, 2233+131, and 2320+079. The dust in these systems could cause the intrinsic QSO fluxes to be underestimated. This in turn can cause  $\log[J(\nu_0)]$  to be underestimated by up to a factor of 3, in addition to the sources of error discussed above (Srianand & Khare 1996). Only six of these objects, 0334-204, 0938+119, 0955+472, 1215+333, 2126-158, and 2233+131, appear in our low luminosity subsample, suggesting that this subsample is not preferentially heavily dust-obscured. Nevertheless, the BDO analysis was performed on all 16 objects exhibiting damped Ly $\alpha$  systems; and found the best fit value for  $\log[J(\nu_0)]$  to be  $-21.45^{+0.40}_{-0.53}$ , a factor of  $1.9^{+8.1}_{-1.6}$  lower than the value obtained for the sample as a whole. This does not allow us to say anything significant about the presence or absence of dust, so we will neglect its influence.

Dividing our line sample into subsamples of high ( $z > 2.5$ ) and low ( $z < 2.5$ ) redshift lines, we find marginal evidence for evolution in the intensity of the background, namely that the maximum likelihood background intensity is lower by a factor of about  $1.9^{+3.9}_{-1.4}$  at lower redshift. The BDO results corroborate this, but with larger uncertainties. The factor by which  $J(\nu_0)$  is found to be lower at lower redshifts is  $2.5^{+27.7}_{-2.2}$ . Gravitational lensing could mimic a trend with redshift with about the same order of magnitude, if the high redshift subsample contains a significant number of unknown lenses. However, Figure 3 suggests little if any trend for high luminosity objects to exist at high redshifts in our sample; and the results of Section 3.2 indicate that the high luminosity objects do show a somewhat stronger proximity effect despite the fact that the measured background at high redshift appears to be *higher*. No other studies have found this evidence of

redshift evolution in the background, so we regard it as tentative; and note that it will be interesting to see in future work if this trend can be shown to be real and if it extends smoothly to the low values of  $J(\nu_0)$  found at redshifts less than 1.5.

Since we find high luminosity objects do not exist preferentially at high redshift in our sample, a simple test can be done to determine whether or not there is a significant number of lensed objects in our sample. If the high luminosity QSOs are indeed intrinsically more luminous, and the proximity effect is a purely photoionization-driven phenomenon, these objects should show a more prominent proximity effect. The results of Section 3.2 suggest this is the case. However, in the analysis, this larger line deficit is normalized to the higher Lyman limit luminosities of this subsample. Therefore, one expects these objects, when analyzed as a separate subsample, to yield a value of  $J(\nu_0)$  that is consistent with that found for low luminosity objects if the values of the QSO fluxes are not in error due to lensing. If the high luminosity QSOs, or a subset of them, are lensed objects, then they are not necessarily intrinsically more luminous than the low luminosity QSOs. In this case, the influence of the lensed objects on the surrounding IGM will be overestimated and given the observed line deficit, the background will also be overestimated. Table 4 lists the results obtained for the high and low luminosity subsamples of our data set. The values obtained for these subsamples are equal within the uncertainties. This is consistent with there being no significant effects from gravitational lensing in our sample.

### 5.1. HI Ionization Rate

We tested a range of values for  $\Gamma$ , the HI ionization rate, using our data. The constant value found to fit the data the best is  $1.9^{+1.2}_{-1.0} \times 10^{-12} \text{ s}^{-1}$ . This value is in reasonable agreement with that predicted by the QSO-dominated model of Haardt & Madau (1996) at this redshift,  $1.0 \times 10^{-12} \text{ s}^{-1}$  ( $q_0=0.5$ ). Using Equation 16 and  $J^Q(\nu) = J^Q(\nu_0)(\frac{\nu}{\nu_0})^{-\alpha}$ , and assuming global QSO spectral indices of 0, 1.5, and 2, the ionization rate found from our data corresponds to  $\log[J(\nu_0)] = -21.34, -21.17,$  and  $-21.12$ , respectively.

The parameter set ( $A, B, z_c, S$ ) found to give the best fit to the data is that of Fardal et al. (1998) for the Q2 luminosity function ( $1.2 \times 10^{-12} \text{ s}^{-1}, 0.58, 2.38, 2.77$ ) which, for a redshift of 2.9 yields an ionization rate of  $2.7 \times 10^{-12} \text{ s}^{-1}$ , in good agreement with our solution, and within a factor of  $\sim 3$  of the Haardt & Madau result. Thus, we conclude that a significant contribution to the ionizing background from stellar UV emission is not required at this redshift.

### 5.2. Curve-of-Growth and Other Systematics

On the basis of a curve-of-growth argument, one might expect that weak lines would show a more prominent proximity effect than strong lines. We have compared the results obtained for a constant equivalent width threshold of  $0.32 \text{ \AA}$  with that obtained for lines with  $0.16 \text{ \AA} < W < 0.32 \text{ \AA}$ . Instead of finding a more pronounced proximity effect for the weak lines, we find a less significant deficit of lines within  $1.5 h^{-1} \text{ Mpc}$  of the QSOs. This deficit is  $4.0\sigma$ , versus  $5.5\sigma$  for lines with  $W > 0.32 \text{ \AA}$ . As Table 4 lists,

the value of  $\log[J(\nu_0)]$  recovered from these weak lines is correspondingly higher than that found using strong lines,  $-20.45^{+0.37}_{-0.90}$  versus  $-21.15^{+0.17}_{-0.43}$ . Cooke et al. (1997) point out that this could be the result of a higher degree of blending of weaker lines compared to strong ones in crowded spectral regions. The background flux measurement will be an overestimate because blending will cause fewer individual lines to be resolved further from the QSO. Because the reduction in line density near the QSO will work to reduce line blending, the overall effect of line blending will be to suppress the true magnitude of the proximity effect causing  $J(\nu_0)$  to be overestimated, by a factor of 4.5 in this case. It is difficult to ascertain whether this effect is as strong for lines with  $W > 0.32 \text{ \AA}$  or whether the curve-of-growth effect discussed in Section 4 which also causes  $J(\nu_0)$  to be overestimated, is more important. We expect that for lines with  $W > 0.32 \text{ \AA}$ , the effects of blending are reduced somewhat, while the curve-of-growth effects will remain a factor.

We have addressed many of the systematics which could possibly have affected our analysis. A treatment of the QSO systemic redshifts was integrated directly into our analysis and was found to influence the  $J(\nu_0)$  found by up to a factor of  $\sim 2$ . Other effects, such as the influences of metals and dust, which can cause  $J(\nu_0)$  to be underestimated, and the influences of lensing, line blending, and curve-of-growth effects, which can cause  $J(\nu_0)$  to be overestimated, were treated after the fact in an attempt to understand the magnitude of their effects on the value of  $J(\nu_0)$  derived. The CLOUDY simulations discussed above indicate that allowing for an absorber metal abundance of  $10^{-2}$  solar has little effect on the value of  $J(\nu_0)$  found from the data. Dust in intervening absorption systems may have affected our result. Though we were unable to quantify this effect with high confidence, it could be on the order of a factor of 2. We assert that QSO flux amplification due to lensing has not significantly biased our result; and we attempt to minimize the effect of blending discussed above by using only lines with  $W > 0.32 \text{ \AA}$ . Our result may be susceptible to the curve-of-growth effect we addressed through the simulations in Section 4. In those simulations, we found that the discrepancy between in the input and recovered values of  $J(\nu_0)$  depended upon the input value of  $J(\nu_0)$  itself. The magnitude of the discrepancy corresponding to the  $J(\nu_0)$  we found from the data was a factor of  $\sim 2$ . We therefore suspect that if our result,  $\log[J(\nu_0)] = -21.15^{+0.17}_{-0.43}$ , is systematically biased in any way, it is an overestimate of the true background and could be in error by up to a factor of 2; though this could be balanced somewhat by systematic error due to dust, which works in the opposite direction.

### 5.3. Comparison with Previous Measurements

Our value for  $J(\nu_0)$  agrees well with other measurements at similar redshift, with the exception of those of B94 and Fernández-Soto et al. (1995) who both derive values four times larger than our best value for  $J(\nu_0)$ ,  $\sim 3 \times 10^{-21} \text{ ergs s}^{-1} \text{ cm}^{-2} \text{ Hz}^{-1} \text{ sr}^{-1}$ . The measurement of B94 does not take into account QSO systemic redshifts, but she notes that if they are blueshifted with respect to Ly $\alpha$  by 1000 km s $^{-1}$ , this would lower the derived value of  $J(\nu_0)$  by a factor of 3, bringing it into reasonable agreement with our result. The Fernández-Soto et al. (1995) value is de-



rived from 3 QSO spectra showing a proximity effect due to foreground QSOs. These authors are not able to place an upper limit on their measurement, but our value of  $7.0 \times 10^{-22}$  ergs s<sup>-1</sup> cm<sup>-2</sup> Hz<sup>-1</sup> sr<sup>-1</sup> for  $J(\nu_0)$  is consistent with their lower limit of  $1.6 \times 10^{-22}$  ergs s<sup>-1</sup> cm<sup>-2</sup> Hz<sup>-1</sup> sr<sup>-1</sup>. In fact, when these authors examine the proximity effect in a single QSO spectrum due to the background  $z \sim 2$  QSO itself, they derive a value for  $J(\nu_0)$  of  $7.9_{-6.0}^{+23}$   $\times 10^{-22}$  ergs s<sup>-1</sup> cm<sup>-2</sup> Hz<sup>-1</sup> sr<sup>-1</sup>, which brings their estimate into better agreement with our values for our total sample and for our low redshift subsample within their large errors. Direct measurements of the background at redshifts  $\sim 3$ -3.5 have been made using long-slit spectroscopy of fields containing optically thick Ly $\alpha$  absorbers in efforts to detect fluorescent emission the absorbers produce from the ionizing radiation field incident upon them (Lowenthal et al. 1990, Martínez-González et al. 1995). Recent Keck telescope observations by Bunker et al. (1998) at  $2.5 < z < 4.1$  have achieved a factor of 2-10 higher sensitivity and place a firmer direct limit on the background than previous work. Their null signal in a 90-minute integration with a 3' slit sets an upper limit on  $J(\nu_0)$  of  $2 \times 10^{-21}$  ergs s<sup>-1</sup> cm<sup>-2</sup> Hz<sup>-1</sup> sr<sup>-1</sup>.

Cooke et al. (1997) claim that the value for the background at  $z \sim 4$  is between their value of  $8.0_{-4.0}^{+8.0} \times 10^{-22}$  ergs s<sup>-1</sup> cm<sup>-2</sup> Hz<sup>-1</sup> sr<sup>-1</sup> and that of Williger et al. (1994),  $1.0$ - $3.0 \times 10^{-22}$  ergs s<sup>-1</sup> cm<sup>-2</sup> Hz<sup>-1</sup> sr<sup>-1</sup>. Our best value of  $J(\nu_0)$  at  $z \sim 3$ ,  $7.0 \times 10^{-22}$  ergs s<sup>-1</sup> cm<sup>-2</sup> Hz<sup>-1</sup> sr<sup>-1</sup>, is in agreement with this, although within the uncertainty there is an allowance for the background to decrease as  $z$  approaches 4.

Table 8 lists these various measurements of  $J(\nu_0)$  in the literature as well as the Kulkarni & Fall (1993) measurement at  $z \sim 0.5$ . Figure 13 also summarizes the literature measurements of  $J(\nu_0)$  from  $z \sim 0.5$  to  $z = 4.5$ .

The solid curves in Figure 13 delineate the evolution of the mean background intensity as a function of redshift for global background source spectral indices between 0 and 2, derived from the Haardt & Madau (1996) model for the HI photoionization rate as a function of redshift discussed in Section 3.6. Over 90% of our sample QSO redshifts lie within the FWHM of the Gaussian in the Haardt & Madau (1996) expression using their best fit parameters. At these redshifts, the Haardt & Madau (1996) curves in Figure 13 are turning over. Nonetheless, for comparison with previous work (B94 and references therein), we investigate a power law redshift dependence of the background intensity:

$$J(\nu_0, z) = J(\nu_0, 0)(1 + z)^j. \quad (19)$$

Using the BDO method, we executed a crude grid search in an attempt to constrain the power law index and normalization of this power law. The lowest  $\chi^2$  (3.86) between the binned data and the BDO photoionization model for a power law background was achieved by  $(j, \log[J(\nu_0, 0)]) = (5.12, -23.97)$ , shown by a dashed line in Figure 14. Extending this solution to low redshift gives  $\log[J(\nu_0, 0.5)] = -23.0$ , in good agreement with the measurement of Kulkarni & Fall (1993). The solution  $(j, \log[J(\nu_0, 0)]) = (-4.16, -18.76)$  gives the next lowest  $\chi^2$  (4.91); and though it also implies mean background intensities over four orders of magnitude too high at low redshift, it traces the Haardt & Madau model at high redshift, giving  $\log[J(\nu_0, 4.5)] =$

21.8, in agreement with the Williger et al. (1994) measurement. It is also shown by a dashed line in Figure 14. Fitting parabolas to the regions near the  $\chi^2$  minima in both  $j$  and  $\log[J(\nu_0, 0)]$  gives the error in each parameter for both of these solutions,  $(5.12 \pm 1.96, -23.97 \pm 1.07)$  and  $(-4.16 \pm 2.36, -18.76 \pm 1.31)$ . B94 found a similarly large range of acceptable solutions:  $-7 < j < 4$  and  $-16.5 < \log[J(\nu_0, 0)] < -23.0$ . The large error bars on these fits indicate that the power law fit to the data is not well-constrained, due possibly to the fact that the mean intensity of the background is turning over at the redshifts of our sample objects, as the Haardt & Madau (1996) model predicts.

#### 5.4. Comparison with Models for the Background

Recent models of the ionizing background include not only the integrated emission from QSOs but also a variety of other physical processes such as star formation in young, high redshift galaxies and attenuation of UV photons by Ly $\alpha$  absorbers and Lyman limit systems (Miralda-Escudé & Ostriker 1990, Madau 1991, 1992, Meiksin & Madau 1993, Haardt & Madau 1996, Fardal et al. 1998). Madau & Shull (1996) find that the production of metals in Ly $\alpha$  absorbers may also be a significant contributor to the UV background at  $z \approx 3$ . Their contribution may be up to  $5 \times 10^{-22}$  ergs s<sup>-1</sup> cm<sup>-2</sup> Hz<sup>-1</sup> sr<sup>-1</sup>, assuming that the bulk of the metals in the Lyman  $\alpha$  forest did not form at  $z \gg 3$ , and assuming a Lyman continuum escape fraction,  $f_{esc}$ , from a galaxy of  $\gtrsim 0.25$ . They note, however, that  $f_{esc}$  is essentially unconstrained.

Past debate about how the space density of QSOs evolves at high redshift (Koo & Kron 1988; Boyle et al. 1991; Irwin et al. 1991; Schmidt et al. 1991; Warren et al. 1994; Kenefick et al. 1995) has been clarified by recent radio surveys (Hook et al. 1995, 1998; Shaver et al. 1996). This work has demonstrated that the space density of radio-loud QSOs decreases rapidly with redshift beyond  $z \sim 3$ . Since these surveys are unaffected by any presence of dust in the intervening IGM; and since they confirm the behavior seen in optically selected surveys, they indicate that the QSO population is truly declining at high redshift. Nevertheless, the discovery of QSOs with redshifts greater than 4 has brought better agreement between the values of  $J(\nu_0)$  found via the proximity effect and the values predicted by the models with QSOs primarily contributing to the background (Madau 1992, Meiksin & Madau 1993, Haardt & Madau 1996).

Madau (1992) and Meiksin & Madau (1993) estimate the QSO UV background by integrating the QSO luminosity function (Boyle 1991) and including the effects of attenuation by hydrogen in the IGM. Their estimates however,  $1$ - $3 \times 10^{-22}$  ergs s<sup>-1</sup> cm<sup>-2</sup> Hz<sup>-1</sup> sr<sup>-1</sup>, are still somewhat lower than the values derived in this paper. The analysis of Haardt & Madau (1996) takes into account the effects of various atomic processes leading to the production of hydrogen-ionizing photons within Ly $\alpha$  absorbers and Lyman limits systems themselves. They conclude that observed QSOs can account for number of ionizing photons required by the proximity effect at  $z \lesssim 4$ . These authors find a value of  $\log[J(\nu_0)]$  equal to  $\sim -21.4$  at  $z = 3$ , in good agreement with the value found in this paper at similar redshifts. The solid lines in Figure 13 show the results from the Haardt & Madau (1996) model for two different values

of the global background source spectral index. The lower and upper curves show the evolution of the background for indices of 0 and 2 respectively. The literature measurements at redshifts between 1.7 and 3.6 agree well with the model predictions. The  $z \sim 0.5$  measurement of Kulkarni & Fall (1993) falls below both model curves and the  $z=4.5$  measurement of Williger et al. (1994) falls above them.

Madau, Haardt, & Rees (1999) revisit the issue of the contribution of high redshift, star-forming galaxies to the ionizing background in light of recent work identifying such objects at  $2 < z < 4$ . (Steidel et al. 1996a,b; Madau et al. 1996; Lowenthal et al. 1997) They calculate the critical photoionization rate necessary to reionize a non-uniform intergalactic medium as a function of redshift. This is compared to the expected contributions from QSOs and young, star-forming galaxies. There are uncertainties in estimating both of these. The QSO luminosity function at  $z > 4$  must be extrapolated from that at lower redshifts. There is also still some debate between theory and observations, eg. of the *Hubble Deep Field*, on the subject of a population of low-luminosity QSOs (see Madau et al. 1999 and references therein) which could cause the QSO luminosity function to steepen with lookback time, making up for the dearth of observed objects at  $z > 4$ . The estimation of the galaxy contribution of ionizing photons is limited by poor knowledge of luminosity function of Lyman-break galaxies at  $z > 4$  as well as by the lack of constraints upon  $f_{esc}$ . Nevertheless, the results are intriguing. Assuming that  $f_{esc}=0.5$ , Madau et al. (1999) find that the contribution of hydrogen-ionizing photons from star-forming galaxies  $z \sim 3$  could exceed that from QSOs by a factor of more than 3. However, the QSO contribution at this redshift is sufficient, according to these estimates, to ionize the IGM at this redshift. Deharveng et al. (1997) estimate a much lower  $f_{esc}$  at  $z=0$ , less than 1%, based on the local galaxy  $H\alpha$  luminosity density. Furthermore, Devriendt et al. (1998) make an independent estimation of the galaxy contribution to  $J(\nu_0)$  assuming damped  $Ly\alpha$  systems to be the progenitors of present day galaxies. Their semi-analytic models include a treatment of not only HI absorption of Lyman limit photons in the intervening IGM, but also of HI and dust absorption in the interstellar medium of the photon-producing galaxies. Their results show that constraining  $f_{esc}$  in this way yields a much lower contribution to the UV background from galaxies at  $z > 2$ . At  $z \sim 2.5$ , their estimated QSO contribution to  $J(\nu_0)$  is 3 orders of magnitude greater than that expected from galaxies. Our measurement of  $J(\nu_0)$  is consistent with the UV background being QSO dominated in the models of both these authors and Haardt & Madau (1996).

In the models of Madau et al. (1999), the scenario changes at  $z \gtrsim 3.5$ . At this redshift, the QSO contribution of ionizing photons falls below the critical limit needed to photoionize the IGM; and by  $z=5$ , it will fall short of the critical value by a factor of  $\sim 4$ . This implies that at high redshift, the contribution from young stars may become the dominant contributor to the background, with the caveat that the space density of star-forming galaxies would have to be maintained at the level observed at  $z \approx 3$ , and that most of their UV photons would have to be free to escape into the IGM. The Devriendt et al. (1998) models lead to the conclusion, however, that the galaxy

contribution to the UV background is negligible at high redshifts.

In conclusion, the proximity effect data at present reflect that the UV background at  $2 < z < 4$  is QSO dominated. The discrepancies between this model at low and high redshifts (Kulkarni & Fall 1993, Williger et al. 1994) indicate that the contribution to the background from galaxies may be of larger relative importance. We plan to undertake an analysis of the proximity effect at low redshifts from a large sample of QSO spectra taken with the Faint Object Spectrograph on the Hubble Space Telescope to place better constraints on the background at  $0.5 < z < 2$ . Further observations of objects at  $z > 4$  are also of particular interest to this subject.

We extend thanks to the staff of the Steward Observatory Bok Telescope for their assistance with the observations, to T. Aldcroft and J. Shields for providing data, to C. Foltz and D. McIntosh for helpful discussions, to J. McDowell for use of his program COLDEN, and to G. Ferland and associates for making the program CLOUDY available for general use. We also thank S. Morris for a helpful referee report. J. S. acknowledges the support of the National Science Foundation Graduate Research Fellowship and the Zonta Foundation Amelia Earhart Fellowship. J. B. acknowledges support from AST-9058510 and AST-9617060 of the National Science Foundation. A. D. acknowledges support from NASA Contract No. NAS8-39073 (ASC). V. P. K. acknowledges partial support from an award from the William F. Lucas Foundation and the San Diego Astronomers' Association. This research has made use of the NASA/IPAC Extragalactic Database (NED) which is operated by the Jet Propulsion Laboratory, California Institute of Technology, under contract with the National Aeronautics and Space Administration.

## REFERENCES

- Bahcall, J. N., Bergeron, J., Boksenberg, A., Hartig, G. F., Jannuzi, B. T., Kirhakos, S., Sargent, W. L. W., Savage, B. D., Schneider, D. P., Turnshek, D. A., Weymann, R. J., & Wolfe, A. M. 1993, *ApJS*, 87, 1
- Bajtlik, S., Duncan, R. C., & Ostriker, J. P. 1988, *ApJ*, 327, 570 (BDO)
- Baker, A. C., Carswell, R. F., Bailey, J. A., Espey, B. R., Smith, M. G., & Ward, M. J. 1994, *MNRAS*, 270, 575
- Baldwin, J. A., Wampler, E. J., & Gaskell, C. M. 1989, *ApJ*, 338, 630
- Barthel, P. D., Miley, G. K., Schilizzi, R. T., & Lonsdale, C. J. 1988, *A&AS*, 73, 515
- Barthel, P. D., Tytler, D. R., & Thomson, B. 1990, *A&A*, 82, 339
- Bechtold, J., Weymann, R. J., Lin, Z., & Malkan, M. A. 1987, *ApJ*, 315, 180 (BWLML)
- Bechtold, J. 1994, *ApJS*, 91, 1 (B94)
- Bohlin, R. C., Savage, B. D., & Drake, J. F. 1978, *ApJ*, 224, 132
- Boroson, T. A. & Green, R. F. 1992, *ApJS*, 80, 109
- Boyle, B. J. 1991 in *Proc. 1990 Texas/ESO-CERN Symp. on Relativistic Astrophysics, Cosmology, and Fundamental Physics*, ed. J. D. Barrow, L. Mestel, & P. A. Thomas (Ann. NY Acad. Sci., 647, 14)
- Boyle, B. J., Jones, L. R. & Shanks, T. 1991, *MNRAS*, 251, 482
- Bremer, M. N. & Johnstone, R. M. 1995, *MNRAS*, 277, L51
- Bunker, A. J., Marleau, F. R., & Graham, J. R. 1998, *AJ*, 116, 2086
- Burbridge, E. M. 1970, *ApJ*, 160, L33
- Carswell, R. F., Whelan, J. A. J., Smith, M. G., Boksenberg, A., & Tytler, D. 1982, *MNRAS*, 198, 91
- Cheng, F. H., Gaskell, C. M., & Koratkar, A. P. 1991, *ApJ*, 370, 487
- Cooke, A. J., Espey, B., & Carswell, R. F. 1997, *MNRAS*, 284, 552
- Corbin, M. R. 1992, *ApJ*, 391, 577
- Corbin, M. R. & Boroson, T. A. 1996, *ApJS*, 107, 69
- Cowie, L. L., Songaila, A., Kim, T. -S., & Hu, E. M. 1995, *AJ*, 109, 1522
- Cristiani, S., D'Odorico, S., Fontana, A., Giallongo, E., & Savaglio, S. 1995, *MNRAS*, 273, 1016
- Deharveng, J. -M., Faisse, Milliard, B., & Le Brun, V. 1997, *A&A*, 325, 1259
- Devriendt, J. E. G., Sethi, S. K., Guideroni, B., & Nath, B. B. 1998, *MNRAS*, 298, 708
- Dobrzycki, A. & Bechtold, J. 1996, *ApJ*, 457, 102 (DB96)
- Dobrzycki, A., Engels, D., & Hagen, H.-J. 1999, *A&A*, 349, L29
- Espey, B., Carswell, R. F., Bailey, J. A., Smith, M. G., & Ward, M. J. 1989, *ApJ*, 342, 666
- Fardal, M. A., Giroux, M. L. & Shull, J. M. 1998, *AJ*, 115, 2206
- Fernández-Soto, A., Barcons, X., Carballo, R., & Webb, J. K. 1995, *MNRAS*, 277, 235
- Francis, P. J. 1996, *Pub. Ast. Soc. Aust.*, 13, 212
- Giallongo, E., Cristiani, S., Fontana, A., & Trevese, D. 1993, *ApJ*, 416, 137
- Giallongo, E., Cristiani, S., D'Odorico, S., Fontana, A., & Savaglio, S. 1996, *ApJ*, 466, 46
- Griffith, M. R., Wright, A. E., Burke, B. F., & Ekers, R. D. 1994, *ApJS*, 90, 179
- Haardt, F. & Madau, P. 1996, *ApJ*, 461, 20
- Hook, I. M., M<sup>c</sup>Mahon, R. G., Patnaik, A. R., Browne, I. W. A., Wilkinson, P. N., Irwin, M. J., & Hazard, C. 1995, *MNRAS*, 273, L63
- Hook, I. M., Shaver, P. A., & M<sup>c</sup>Mahon, R. G. 1998, in *The Young Universe*, ed. S. D'Odorico, A. Fontana, & E. Giallongo, (San Francisco: ASP), 17
- Hu, E. M., Kim, T. -S., Cowie, L. L., & Songaila, A. 1995, *AJ*, 110, 1526
- Irwin, M., M<sup>c</sup>Mahon, R. G., & Hazard, C. 1991, in *Space Distribution of Quasars*, ed. D. Crampton (San Francisco: ASP), 117
- Johnson, H. L. 1966, *ARA&A*, 4, 193
- Johnson, H. L. 1966, *ARA&A*, 4, 193
- Kennefick, J. D., Djorgovski, S. G., & de Carvalho, R. R. 1995, *AJ*, 110, 2553
- Koo, D. C. & Kron, R. G. 1988, *ApJ*, 325, 92
- Koratkar, A. P., Kinney, A. L., & Bohlin, R. C. 1992, *ApJ*, 400, 435
- Kuhn, O. 1996, Ph.D. thesis, Harvard Univ.
- Kulkarni, V. P. & Fall, S. M. 1993, *ApJ*, 413, L63 (KF93)
- Kunth, D., Sargent, W. L. W., & Kowal, C. 1981, *A&AS*, 44, 229
- Lanzetta, K. M., Turnshek, D. A., & Sandoval J. 1993, *ApJS*, 84, 109
- Laor, A., Bahcall, J. N., Januzzi, B. T., Schneider, D. P., Green, R. F., & Hartig, G. F. 1994, *ApJ*, 420, 110
- Laor, A., Bahcall, J. N., Januzzi, B. T., Schneider, D. P., & Green, R. F. 1995, *ApJS*, 99, 1
- Lowenthal, J. D., Hogan, C. J., Leach, R. W. & Schmidt, G. D. 1990, *ApJ*, 357, 3
- Lowenthal, J. D., Koo, D. C., Guzman, R., Gallego, J., Phillips, A. C., Faber, S. M., Vogt, N. P., Illingworth, G. D., & Gronwall, C. 1997, *ApJ*, 481, 673
- Lu, L., Wolfe, A. M., & Turnshek, D. A. 1991, *ApJ*, 367, 19 (LWT)
- Lynds, C. R. 1971, *ApJ*, 164, L73
- MacAlpine, G. M. & Feldman, F. R. 1982, *ApJ*, 261, 412
- Madau, P. 1991, *ApJ*, 376, L33
- Madau, P. 1992, *ApJ*, 389, L1
- Madau, P. & Shull, J. M. 1996, *ApJ*, 457, 551
- Madau, P., Pozzetti, L., & Dickinson, M. 1998, 498, 106
- Madau, P., Haardt, F., & Rees, M. J. 1999, *ApJ*, 514, 648
- Martínez-González, E., González-Serrano, J. I., Cayón, L., Sanz, J. L., & Martín-Mirónes, J. M. 1995, *A&A*, 303, 379
- M<sup>c</sup>Intosh, D. H., Rieke, M., Rix, H. -W., Foltz, C. B., & Weymann, R. J. 1999a, *ApJ*, 514, 40
- M<sup>c</sup>Intosh, D. H., Rix, H. -W., Rieke, M., Foltz, C. B. 1999b, *ApJ*, 517L, 73
- Meiksin, A. & Madau, P. 1993, *ApJ*, 412, 34
- Miralda-Escudé, J. & Ostriker, J. P. 1990, *ApJ*, 350, 1
- Murdoch, H. S., Hunstead, R. W., Pettini, M., & Blades, J. C. 1986, *ApJ*, 309, 19 (MHPB)
- Nandy, K., Thompson, G. I., Jamar, C., Monfils, A., & Wilson, R. 1975, *ã*, 44, 195
- Nishihara, E., Yamashita, T., Yoshida, M., Watanabe, E., Okumura, S.-I., Mori, A., & Iye, M. 1997, *ApJ*, 488, L27
- Pei, Y. C., Fall, S. M., & Bechtold, J. 1991, *ApJ*, 378, 6
- Pei, Y. C. 1995, *ApJ*, 438, 623
- Perez, E., Penston, M. V., & Moles, M. 1989, *MNRAS*, 239, 55
- Rauch, M., Miralda-Escudé, J., Sargent, W. L. W., Barlow, T., Weinberg, D. H., Hernquist, L., Katz, N., Cen, R., Ostriker, J. P. 1997, *ApJ*, 489, 7
- Sargent, W. L. S., Young, P. J., Boksenberg, A., & Tytler, D. 1980, *ApJS*, 42, 41
- Sargent, W. L. S., Boksenberg, A., & Steidel, C. C. 1988, *ApJS*, 68, 539
- Sargent, W. L. S., Steidel, C. C., & Boksenberg, A. 1989, *ApJS*, 69, 703
- Shaver, P. A., Wall, J. V., Kellermann, K. I., Jackson, C. A., & Hawkins, M. R. S. 1996, *Nature*, 384, 439
- Schmidt, M. & Olsen, E. T. 1968, *AJ*, 73, S117
- Schmidt, M., Schneider, D. P., & Gunn, J. E. 1986, *ApJ*, 310, 518
- Schmidt, M., Schneider, D. P., & Gunn, J. E. 1991, in *Space Distribution of Quasars*, ed. D. Crampton (San Francisco: ASP), 109
- Scott, J., Bechtold, J., & Dobrzycki, A. 2000, *ApJ*, in press (Paper I)
- Seaton, M. J. 1979, *MNRAS*, 187, 73P
- Srianand, R. & Khare, P. 1996, *MNRAS*, 280, 767
- Stark, A. A., Gammie, C. F., Wilson, R. W., Bally, J., Linke, R. A., Heiles, C., & Hurwitz, M. 1992, *ApJS*, 79, 77
- Steidel, C. C. & Sargent, W. L. S. 1991, *ApJ*, 382, 433
- Steidel, C. C., Giavalisco, M., Dickinson, M., & Adelberger, K. L. 1996b, *AJ*, 112, 352
- Steidel, C. C., Giavalisco, M., Pettini, M., Dickinson, M., & Adelberger, K. L. 1996a, *ApJ*, 462, L17
- Tytler, D. 1987, *ApJ*, 321, 69
- Tytler, D. & Fan, X. -M. 1992, *ApJS*, 79, 1
- Tytler, D. & Fan, X. -M. 1994, *ApJ*, 424, L87
- Uomoto, A. 1984, *ApJ*, 284, 497
- Warren, S. J., Hewett, P. C., & Osmer, P. S. 1994, *ApJ*, 421, 412
- Weymann, R. J., Carswell, R. F., & Smith, M. G. 1981, *ARA&A*, 19, 41
- Williams, D. M., Thompson, C. L., Rieke, G. H., & Montgomery, E. F. 1993, *SPiE*, 1946, 482
- Williger, G. M., Baldwin, J. A., Carswell, R. F., Cooke, A. J., Hazard, C., Irwin, M. J., M<sup>c</sup>Mahon, R. G., & Storrie-Lombardi, L. J. 1994, *ApJ*, 428, 574
- Wills, B. J. & Wills, D. 1979, *ApJS*, 41, 689
- Young, P. J., Sargent, W. L. W., & Boksenberg, A. 1982a, *ApJ*, 252, 10.
- Young, P. J., Sargent, W. L. W., & Boksenberg, A. 1982b, *ApJS*, 48, 455
- Zheng, W., Kriss, G. A., Telfer, R. C., Grimes, J. P., & Davidsen, A. F. 1997, *ApJ*, 474, 469

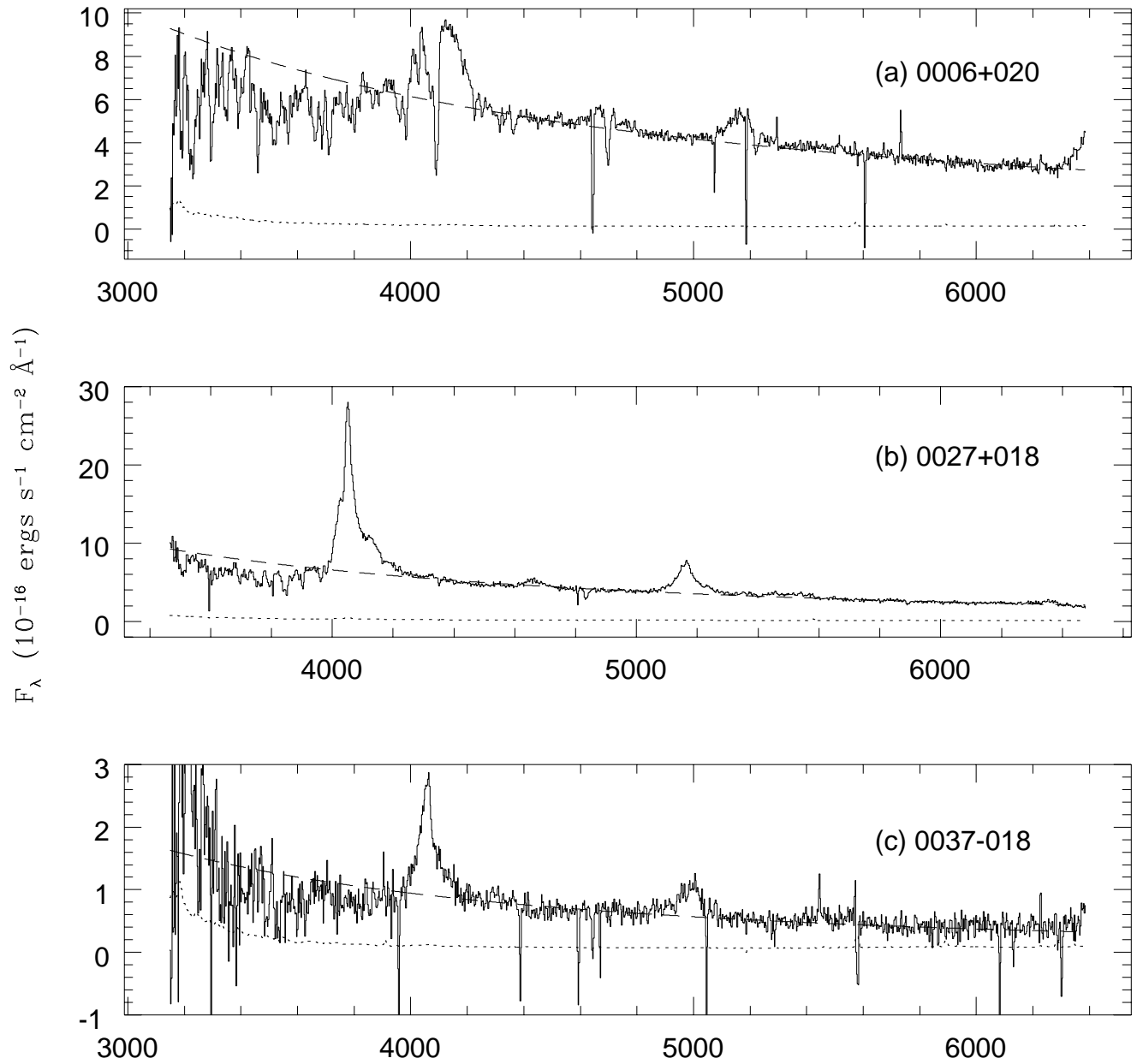
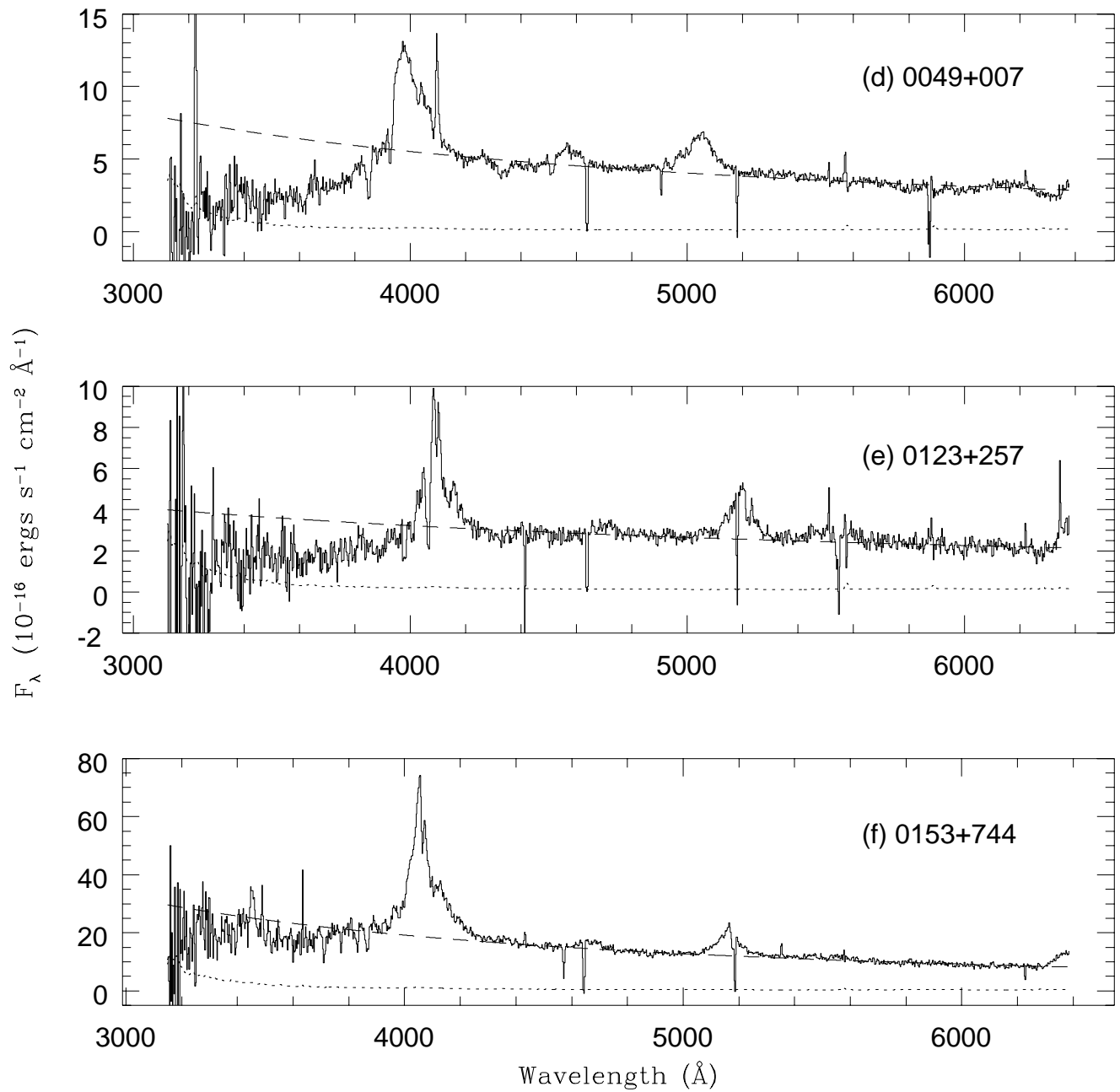
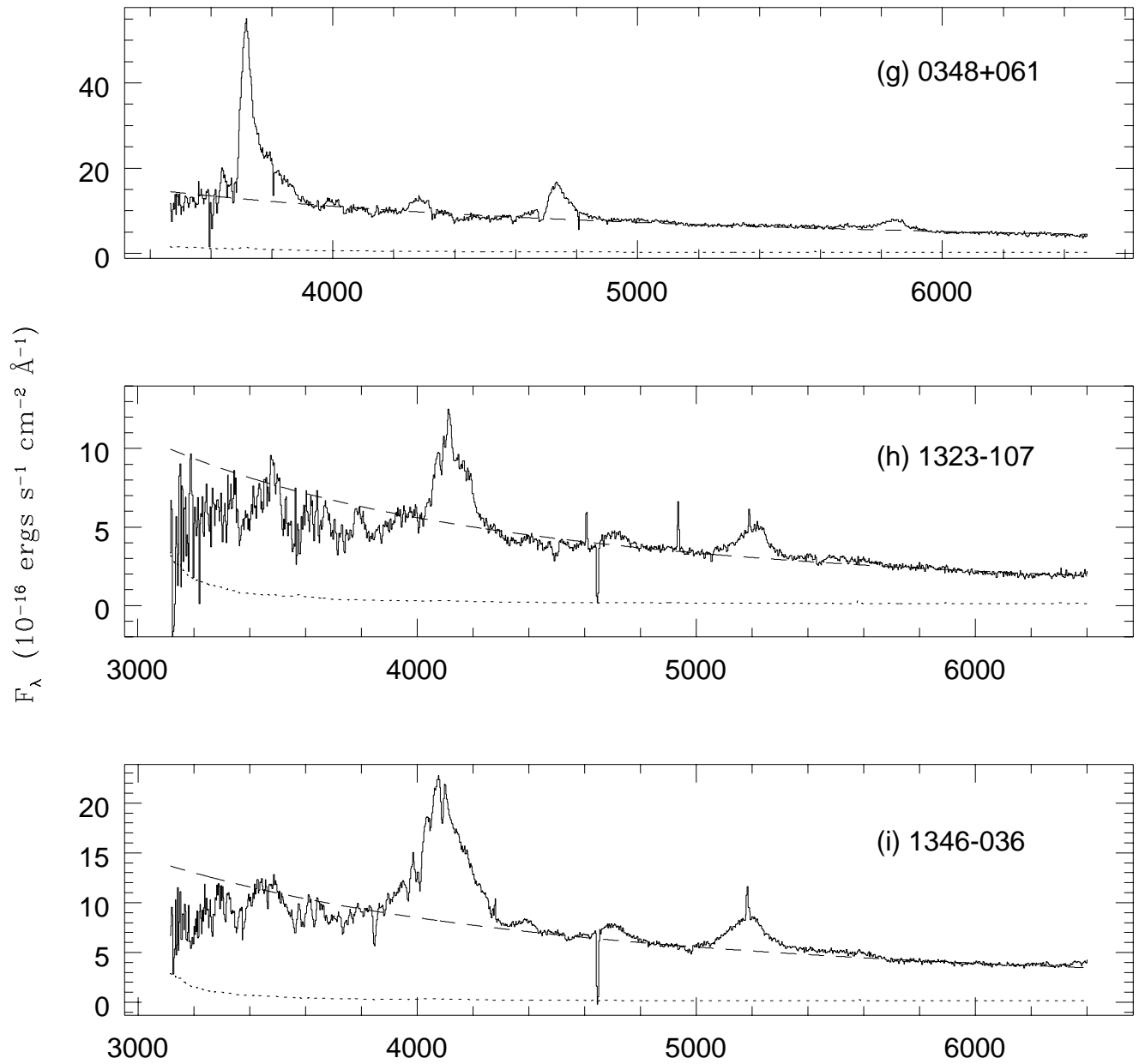
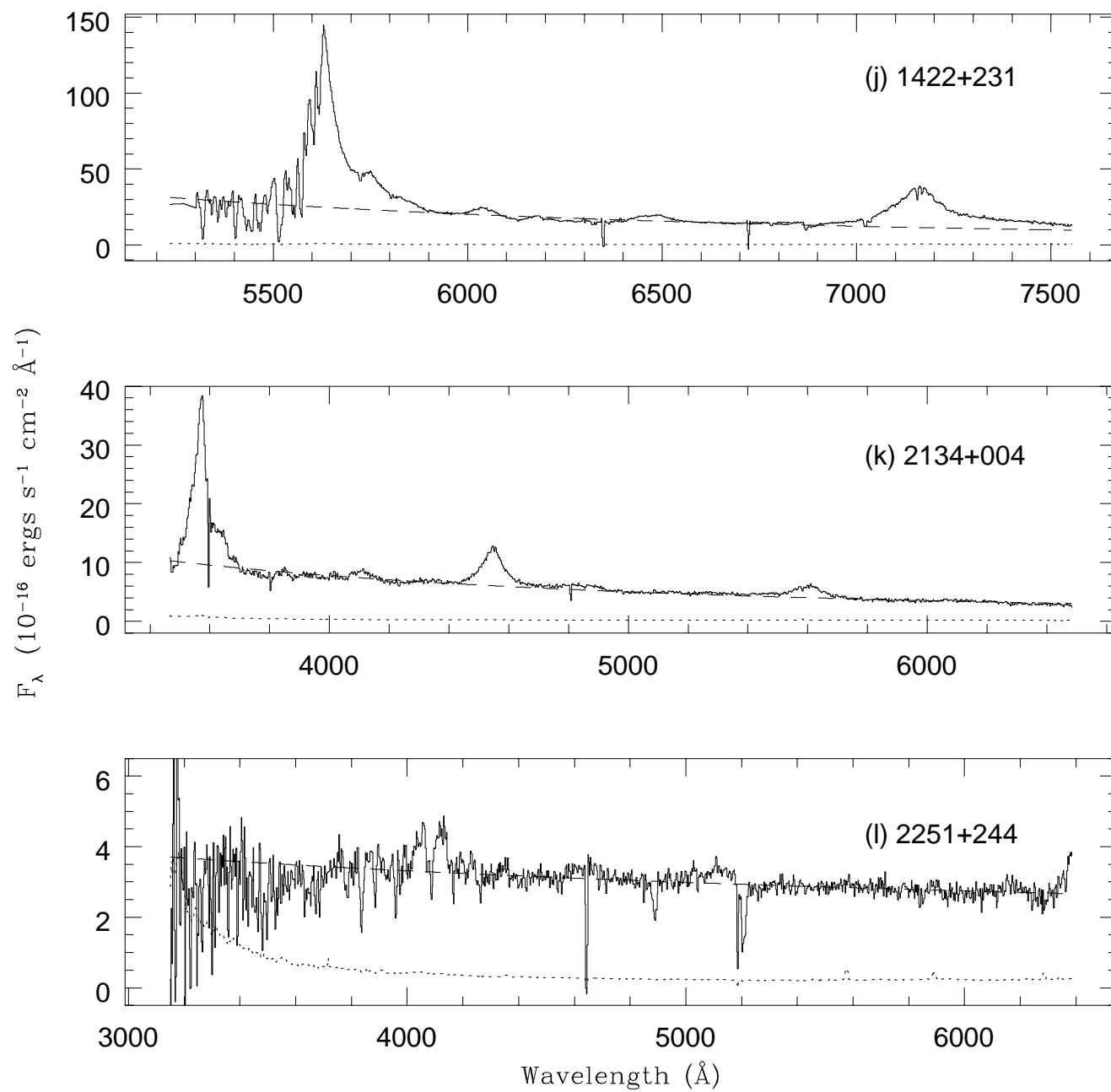
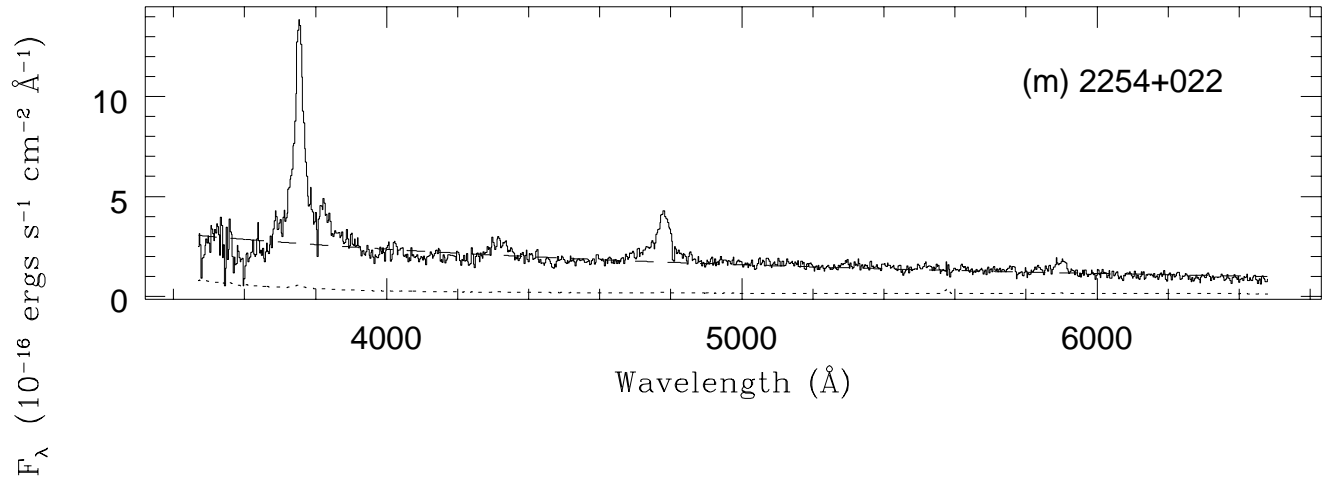


FIG. 1.— Spectrophotometry of  $z \approx 2$  QSOs; Dashed line indicates the power law continuum fit; dotted line indicates the  $1\sigma$  errors











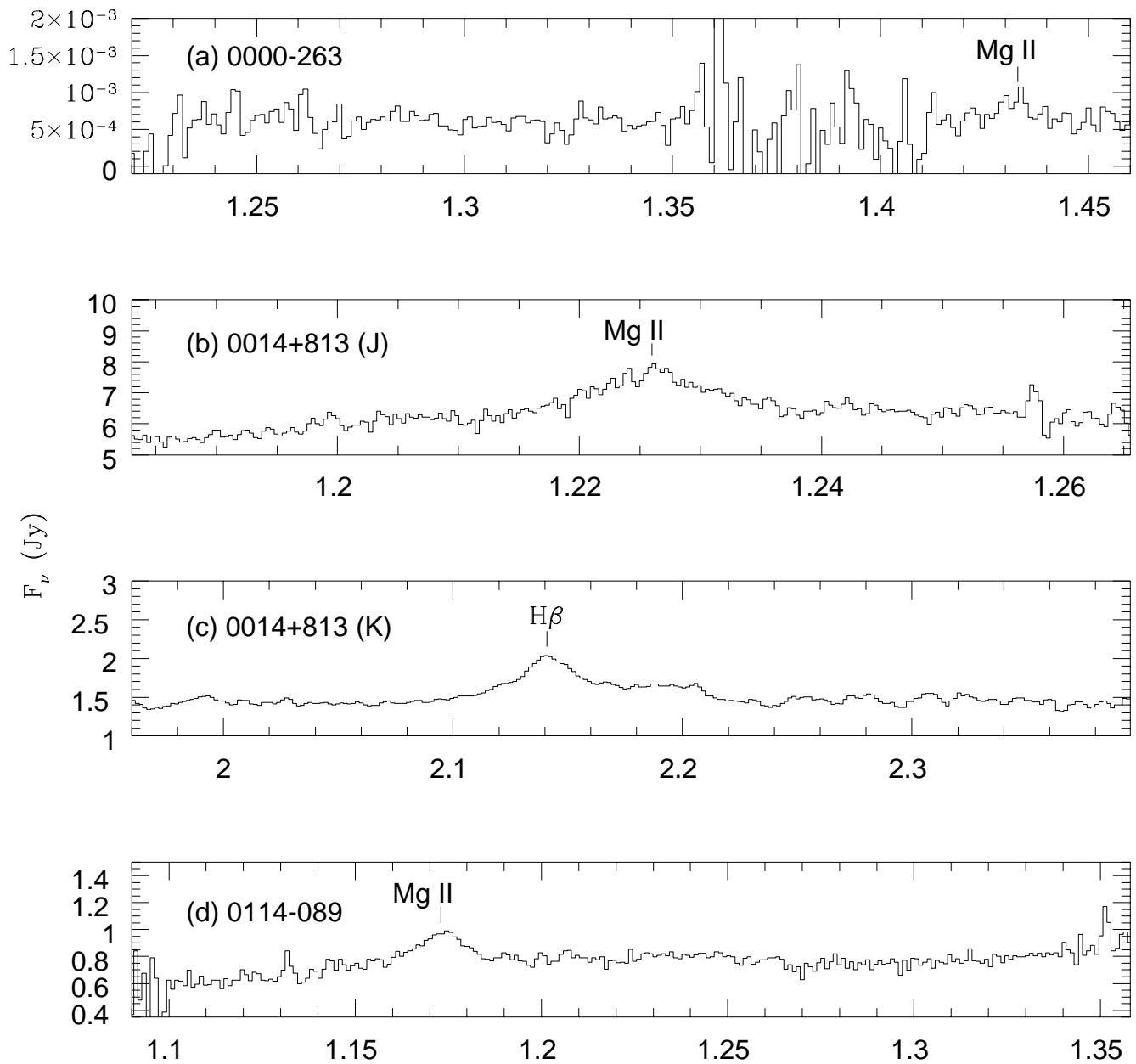
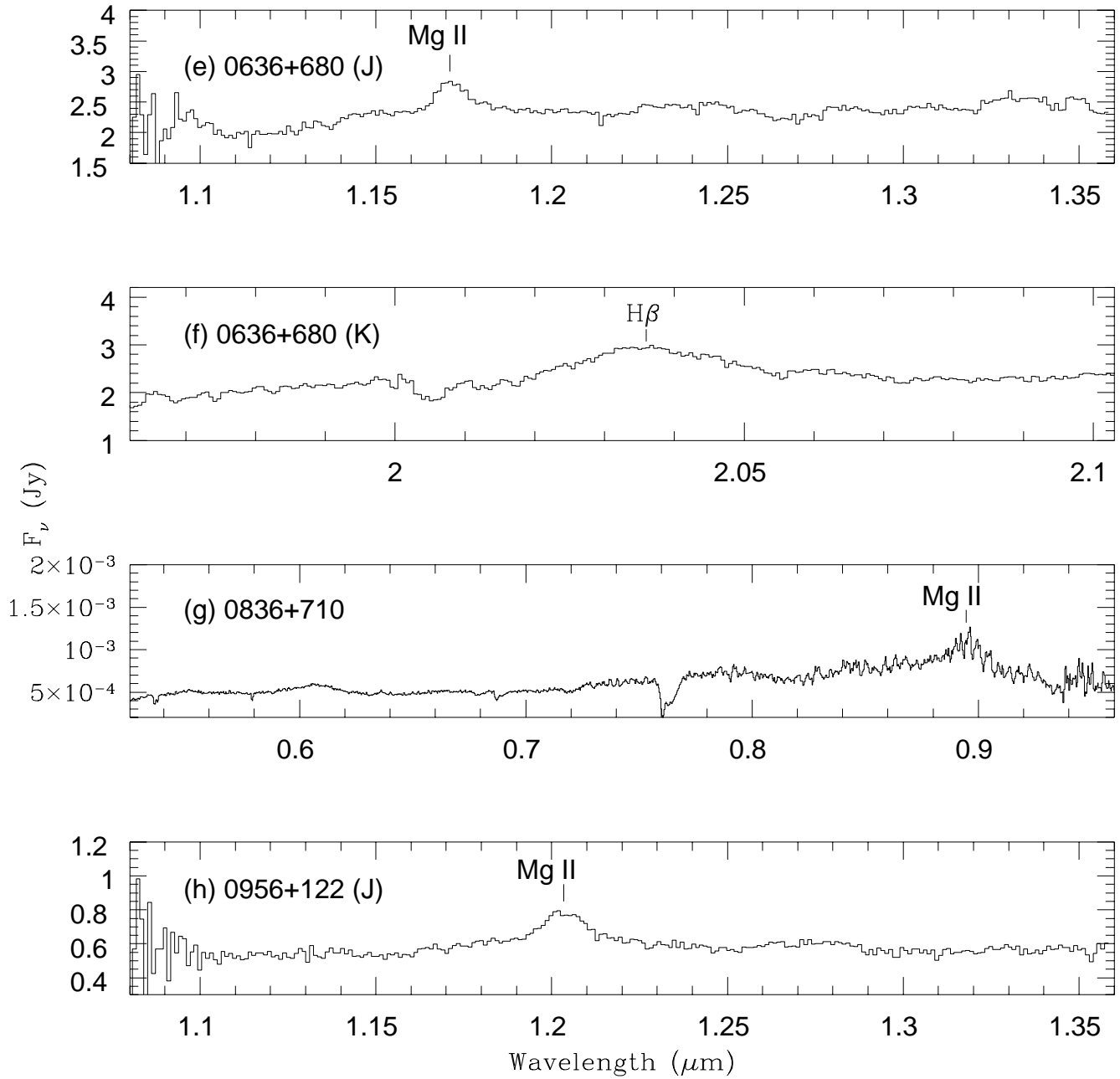
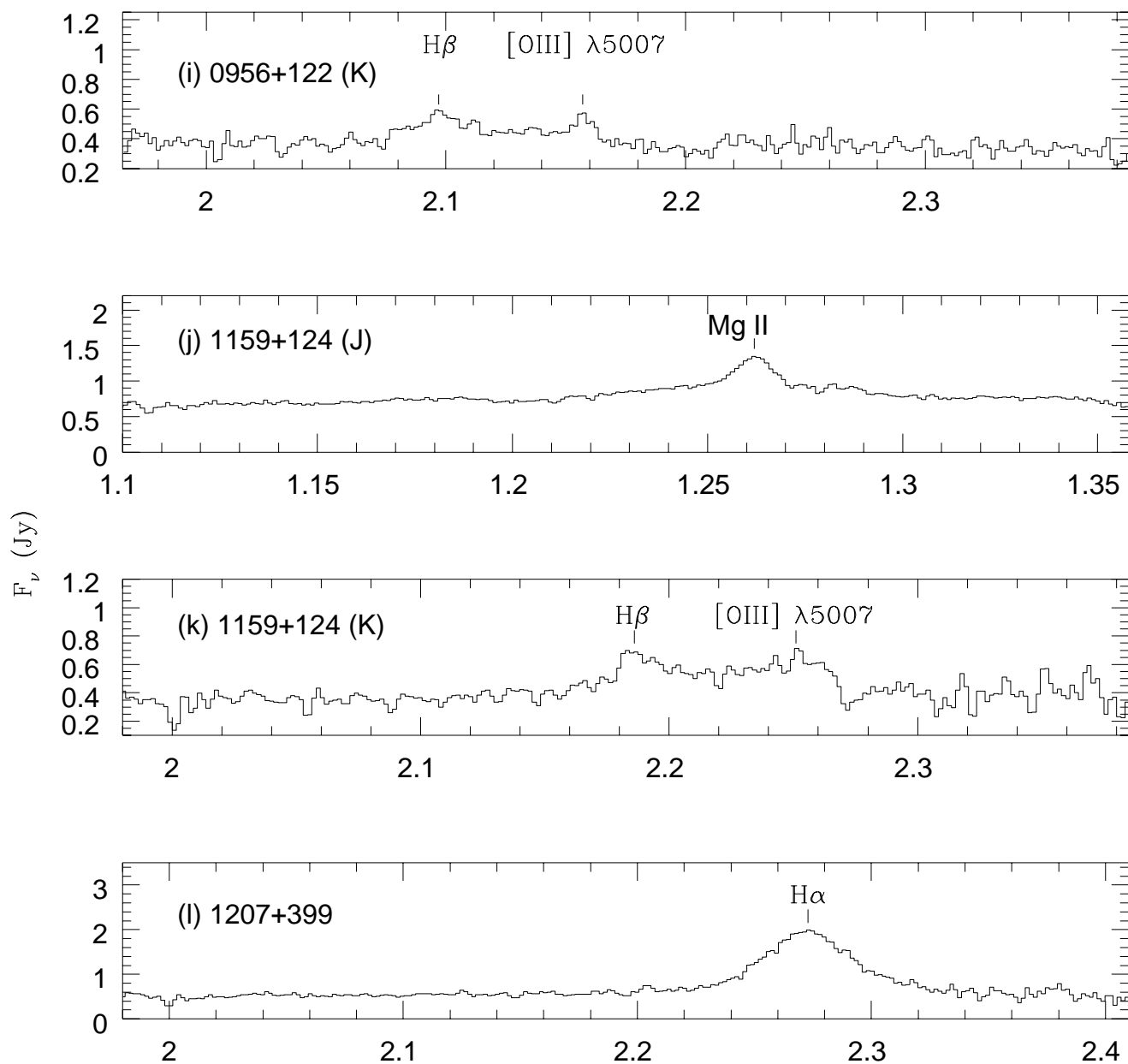
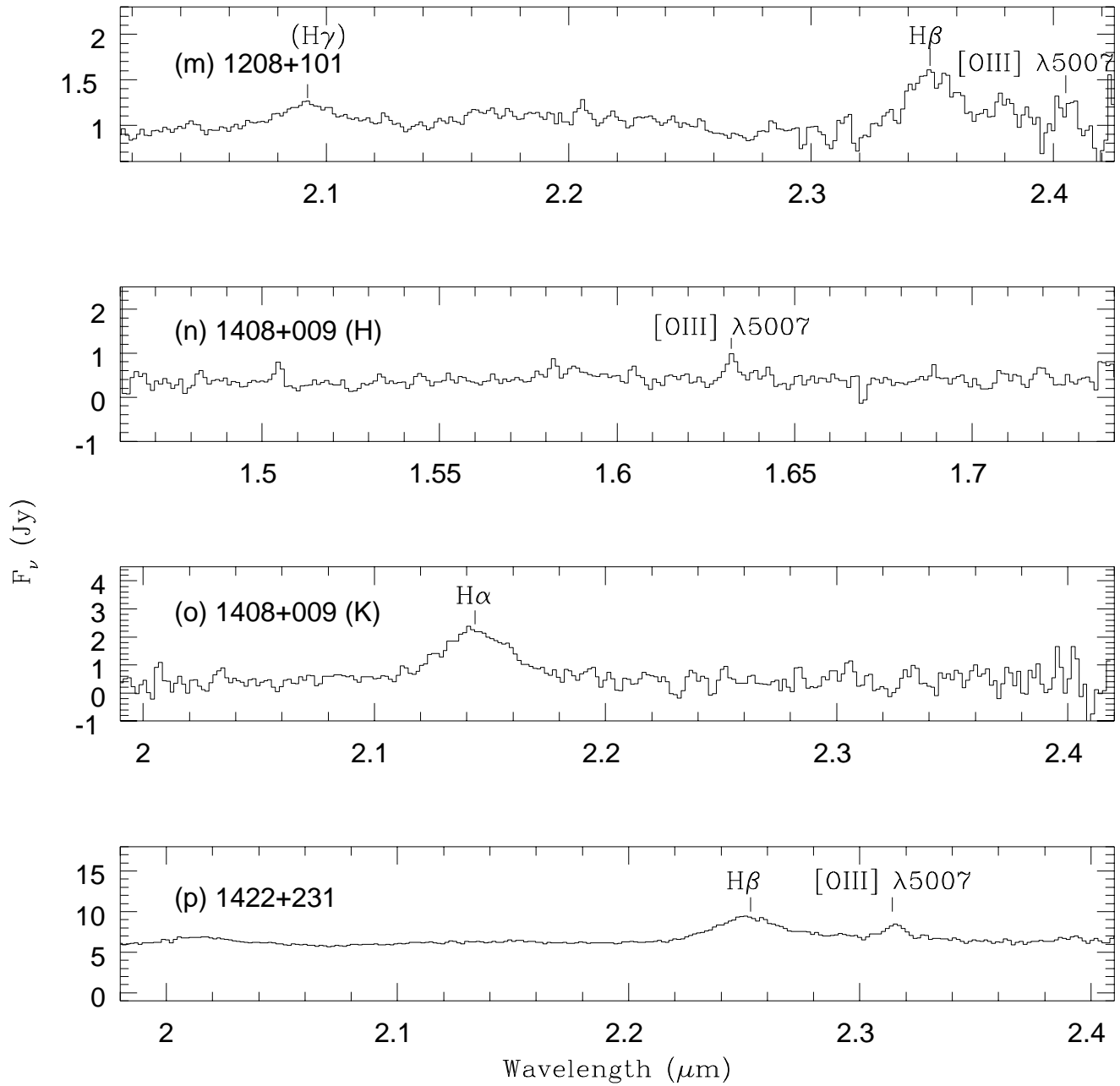
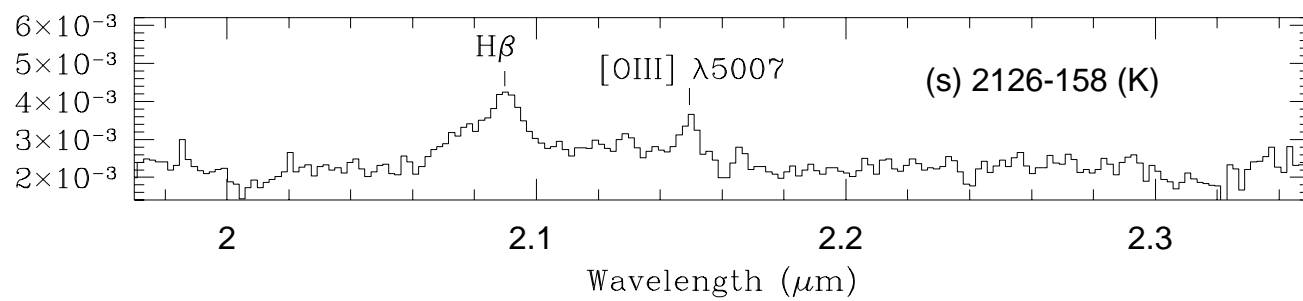
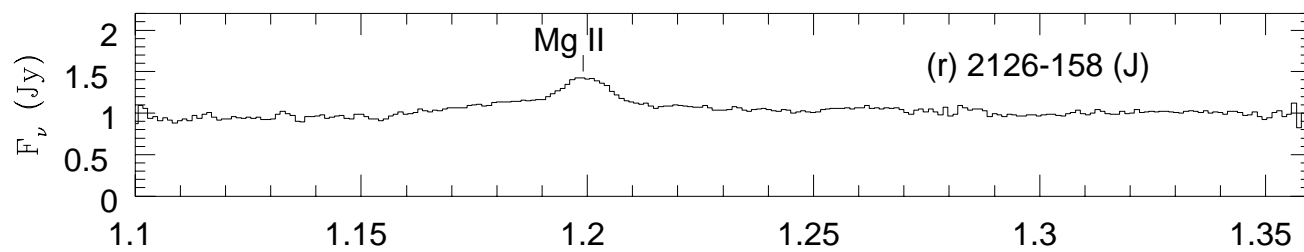
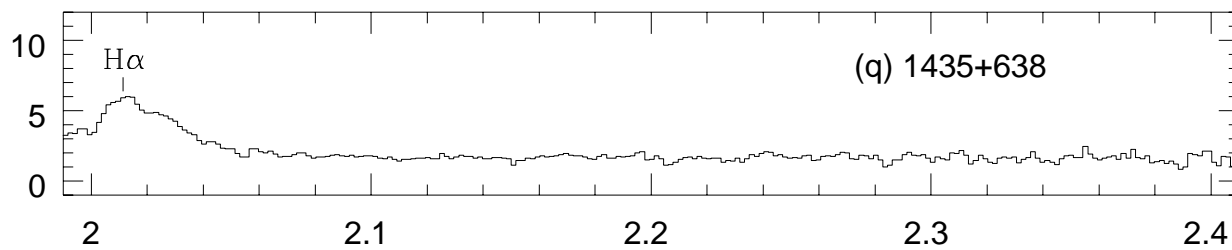


FIG. 2.— Infrared QSO spectra, line identifications as listed in Table 5 are marked









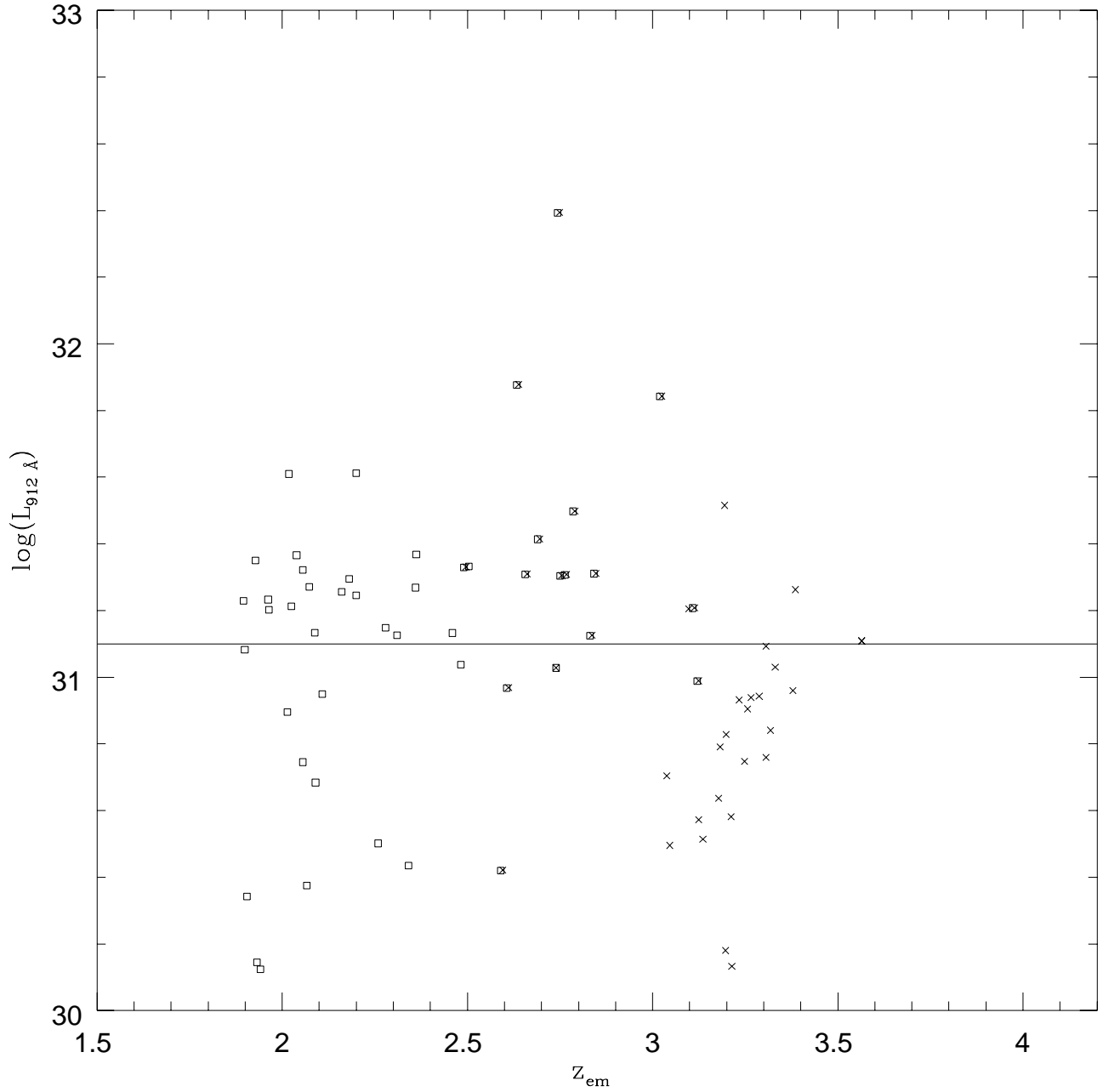


FIG. 3.— Lyman limit luminosity versus redshift for the proximity effect dataset; squares- QSOs from which low redshift line sample was taken; crosses- QSOs from which high redshift line sample was taken; the line marks the boundary between low and high luminosity QSOs

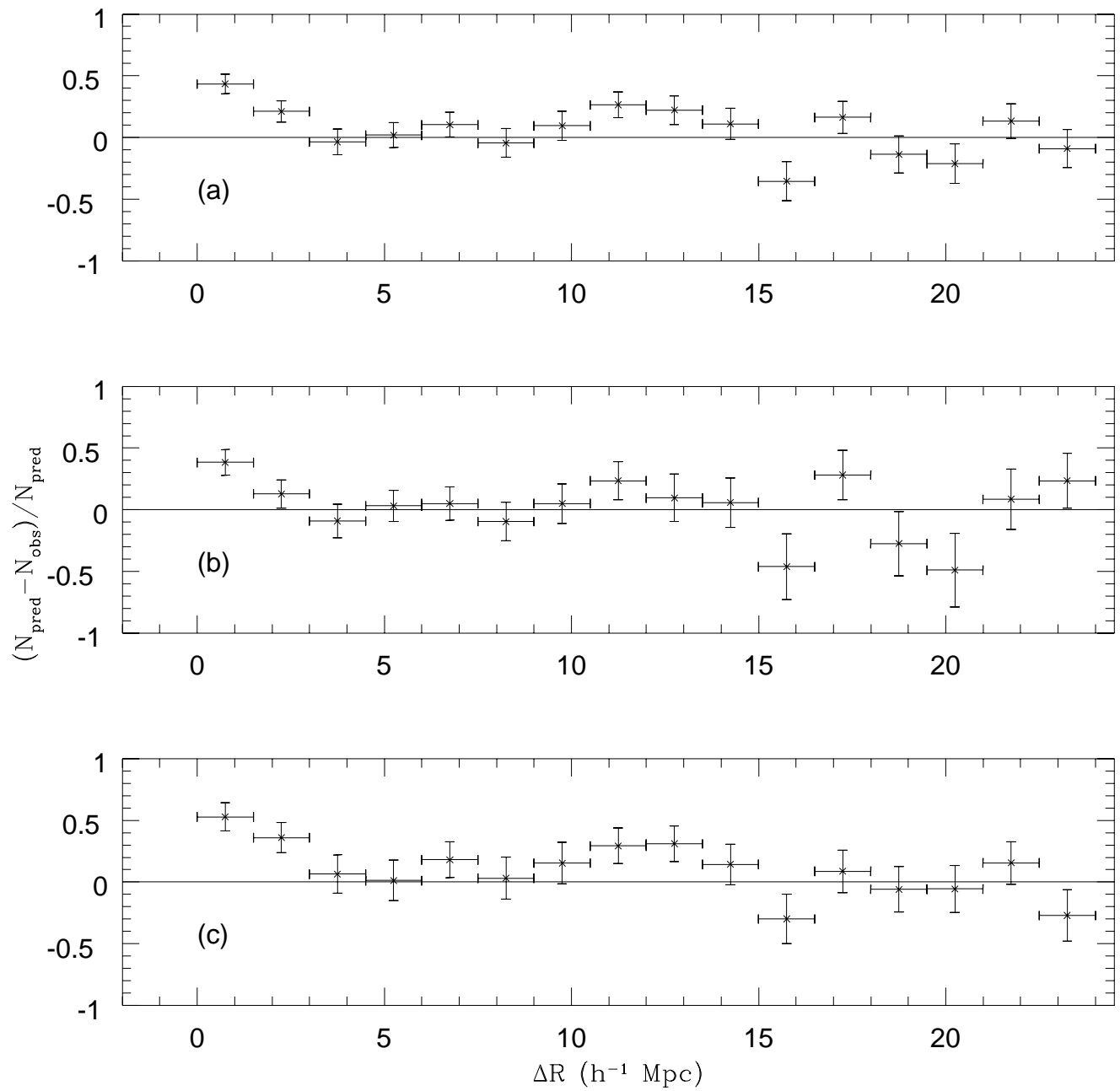


FIG. 4.— Relative deficit of lines with respect to the number predicted by Equ. 1 versus distance from the QSO for lines with rest equivalent width greater than  $0.32 \text{ \AA}$  (a) total sample; (b) low luminosity QSOs; (c) high luminosity QSOs

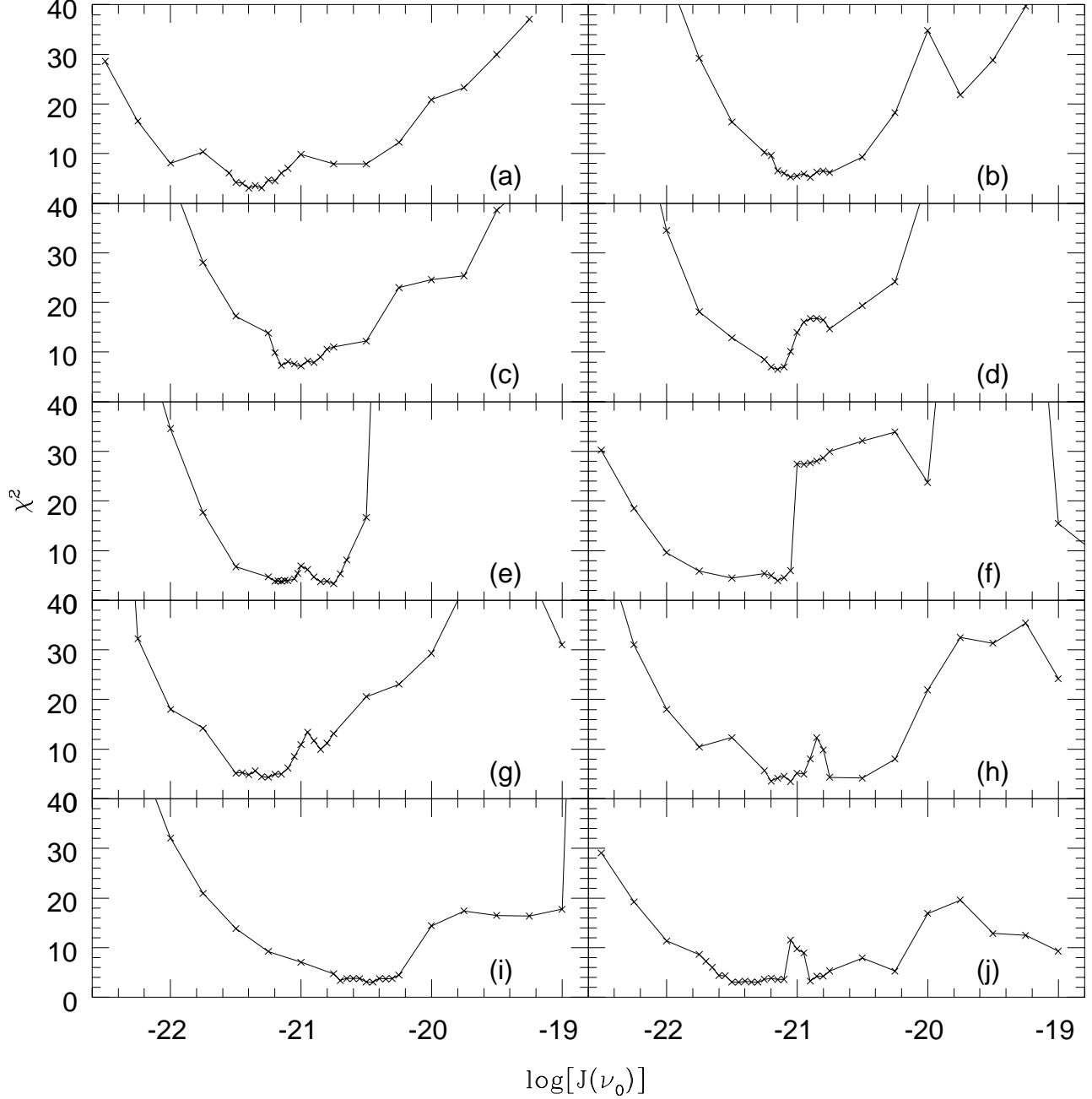


FIG. 5.—  $\chi^2$  of binned data with respect to the ionization model with a constant  $J(\nu_0)$  versus  $\log[J(\nu_0)]$ : (a) DB96 sample; (b) all lines, Ly $\alpha$  QSO redshifts; (c) all lines, using narrow line redshifts where available, Ly $\alpha$  redshifts otherwise; (d) all lines, narrow line redshifts where available, Ly $\alpha$  redshifts + 400 km s $^{-1}$  otherwise; (e) high z lines, QSO redshifts as in case (d); (f) low z lines, QSO redshifts as in case (d); (g) high luminosity QSOs, QSO redshifts as in case (d); (h) low luminosity QSOs, QSO redshifts as in case (d); (i) weak lines only:  $0.16 \text{ \AA} < W < 0.32 \text{ \AA}$ , QSO redshifts as in case (d); (j) lines from QSOs with damped Ly $\alpha$  systems only, QSO redshifts as in case (d)



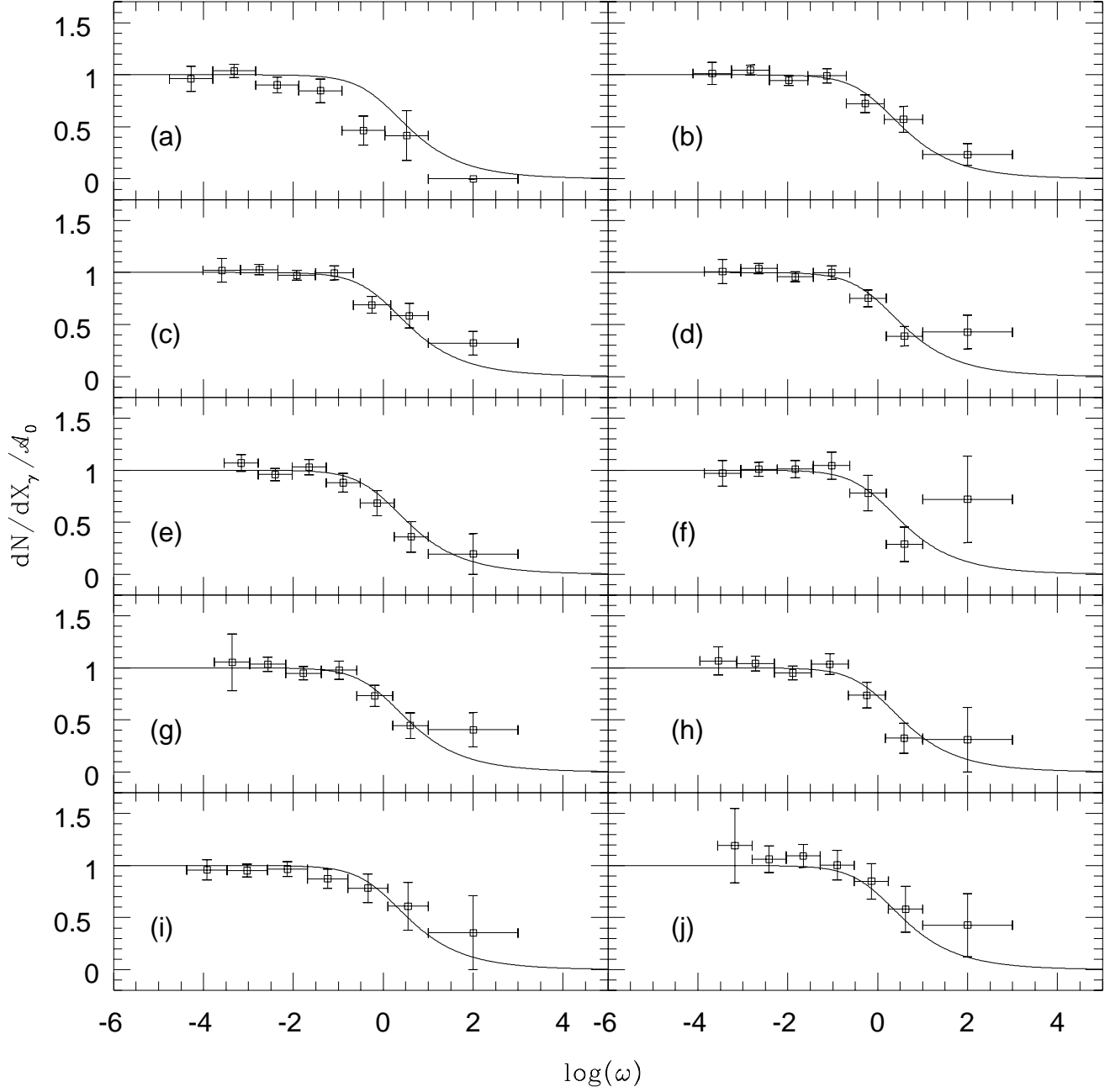


FIG. 6.— Number distribution per coevolving redshift coordinate for the best fit values of  $J(\nu_0)$  (BDO method); (a-j) same as Fig. 5

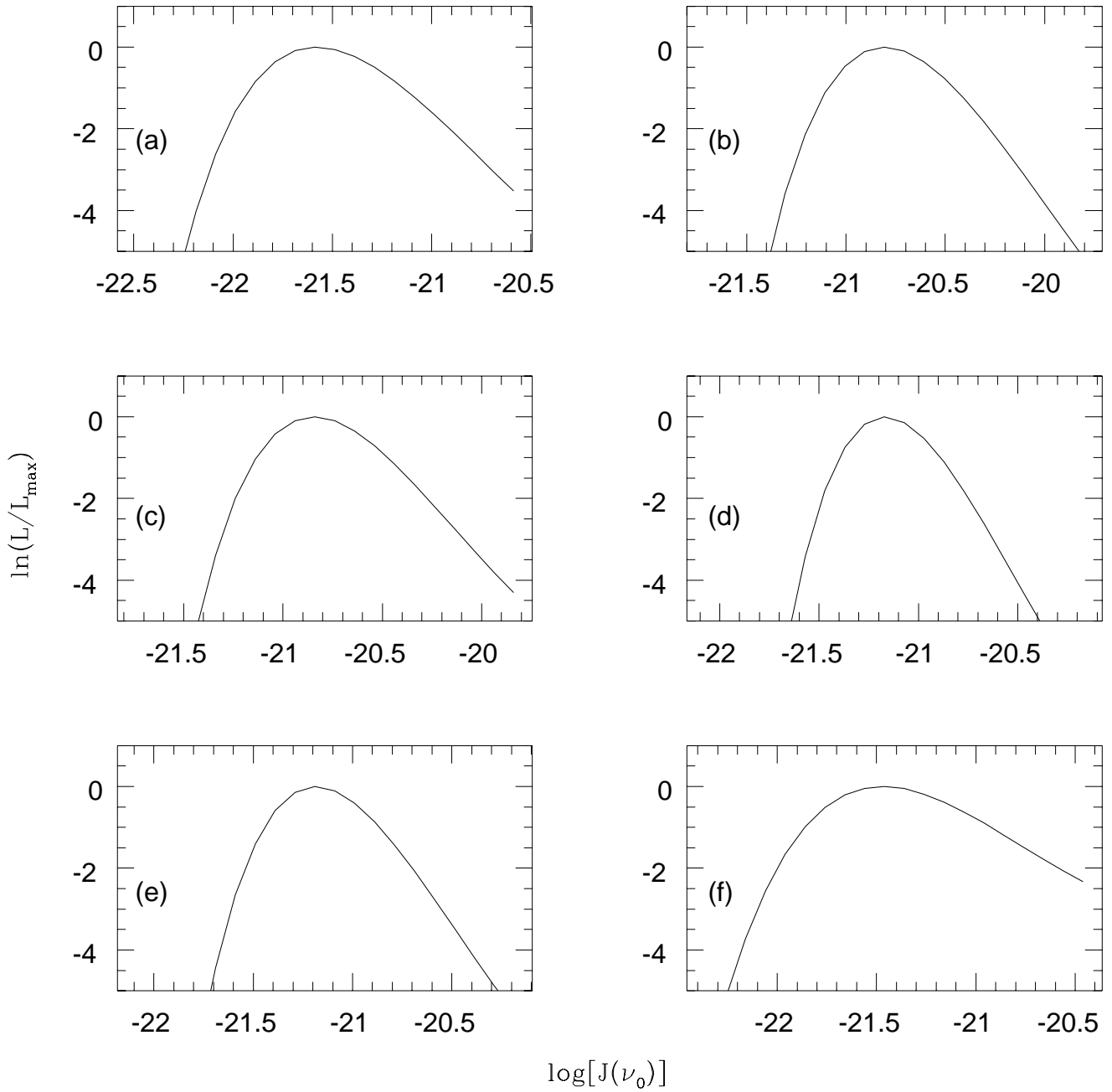


FIG. 7.— Likelihood function versus  $\log[J(\nu_0)]$ ; (a-f) same as Fig. 5

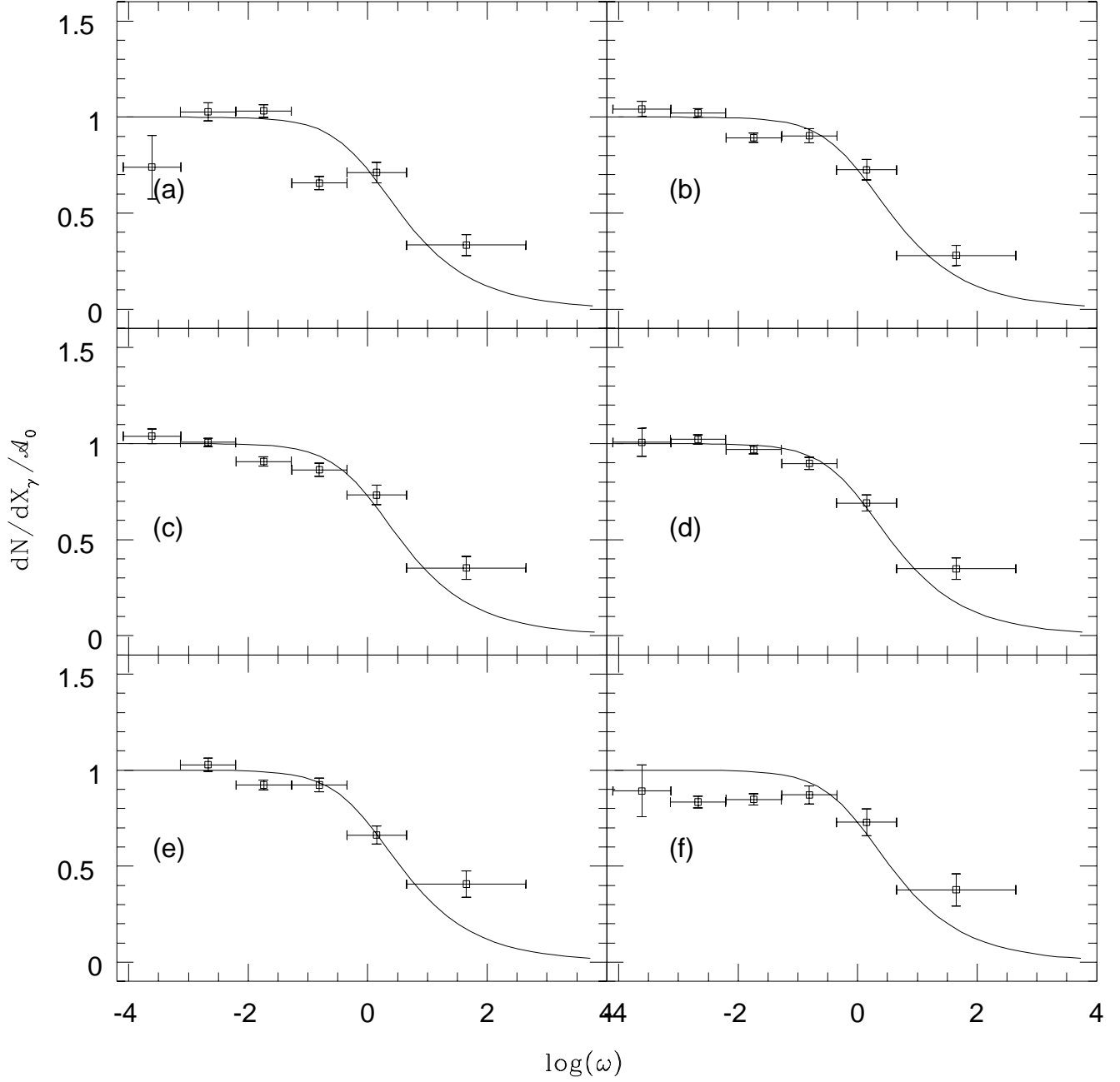


FIG. 8.— Number distribution per coevolving redshift coordinate for the best fit values of  $J(\nu_0)$  (KF method); (a-f) same as Fig. 5

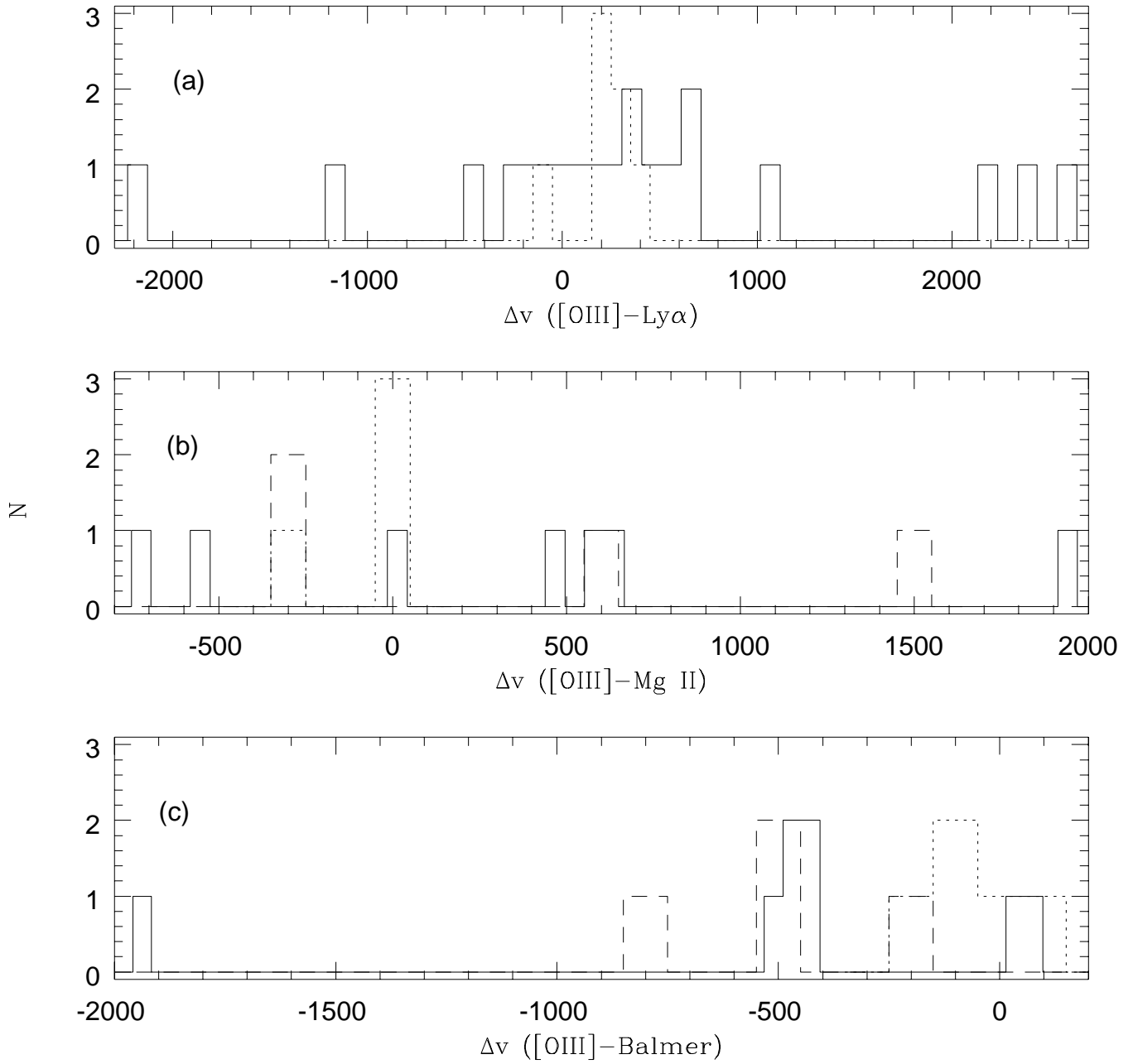


FIG. 9.— Histograms of redshift differences with respect to the [OIII]  $\lambda 5007$  line (a) Ly $\alpha$ ; (b) Mg II; (c) Balmer lines ; dotted lines- data of Laor et al. (1995), dashed lines- data of Nishihara et al. (1997)

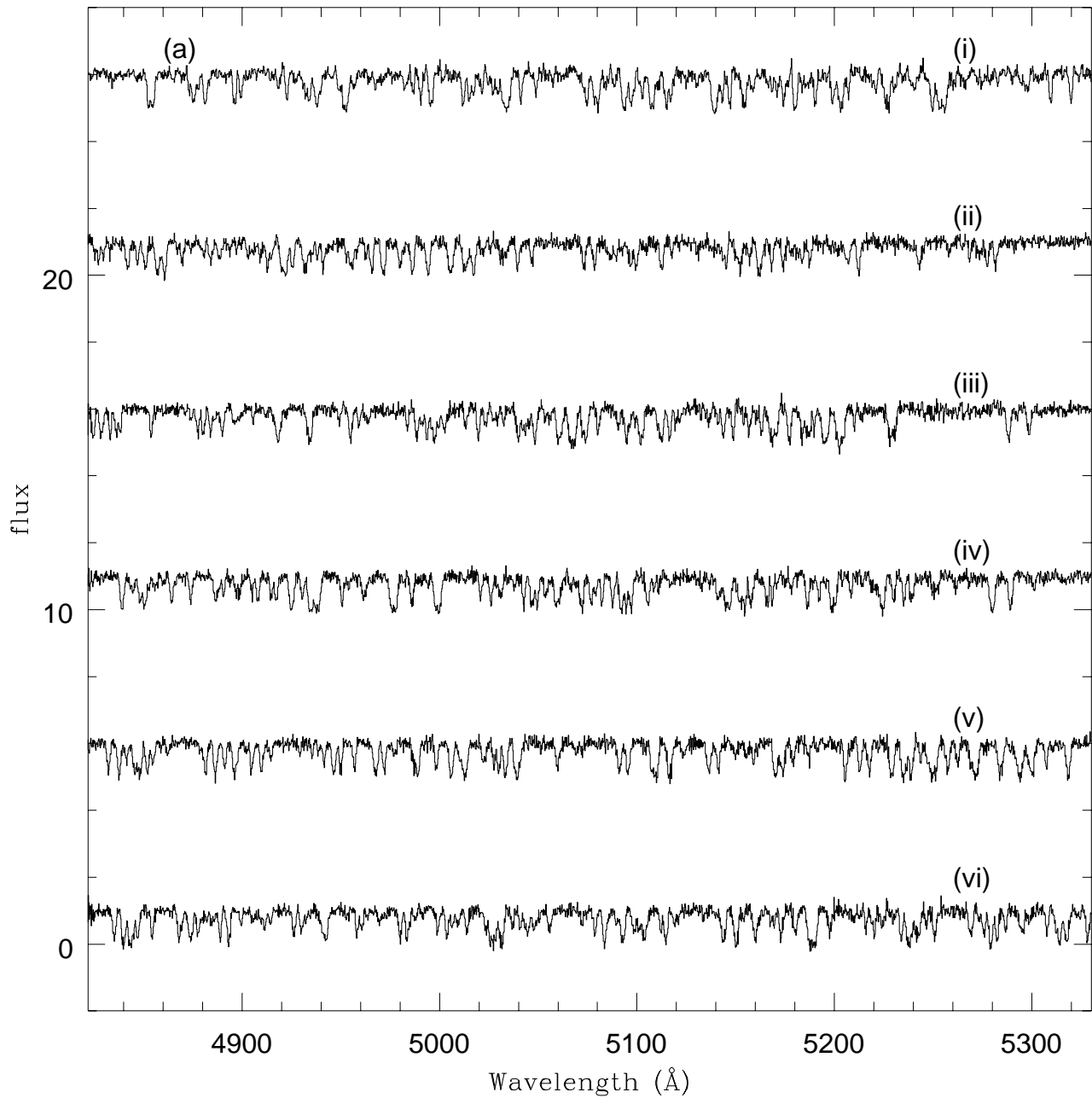
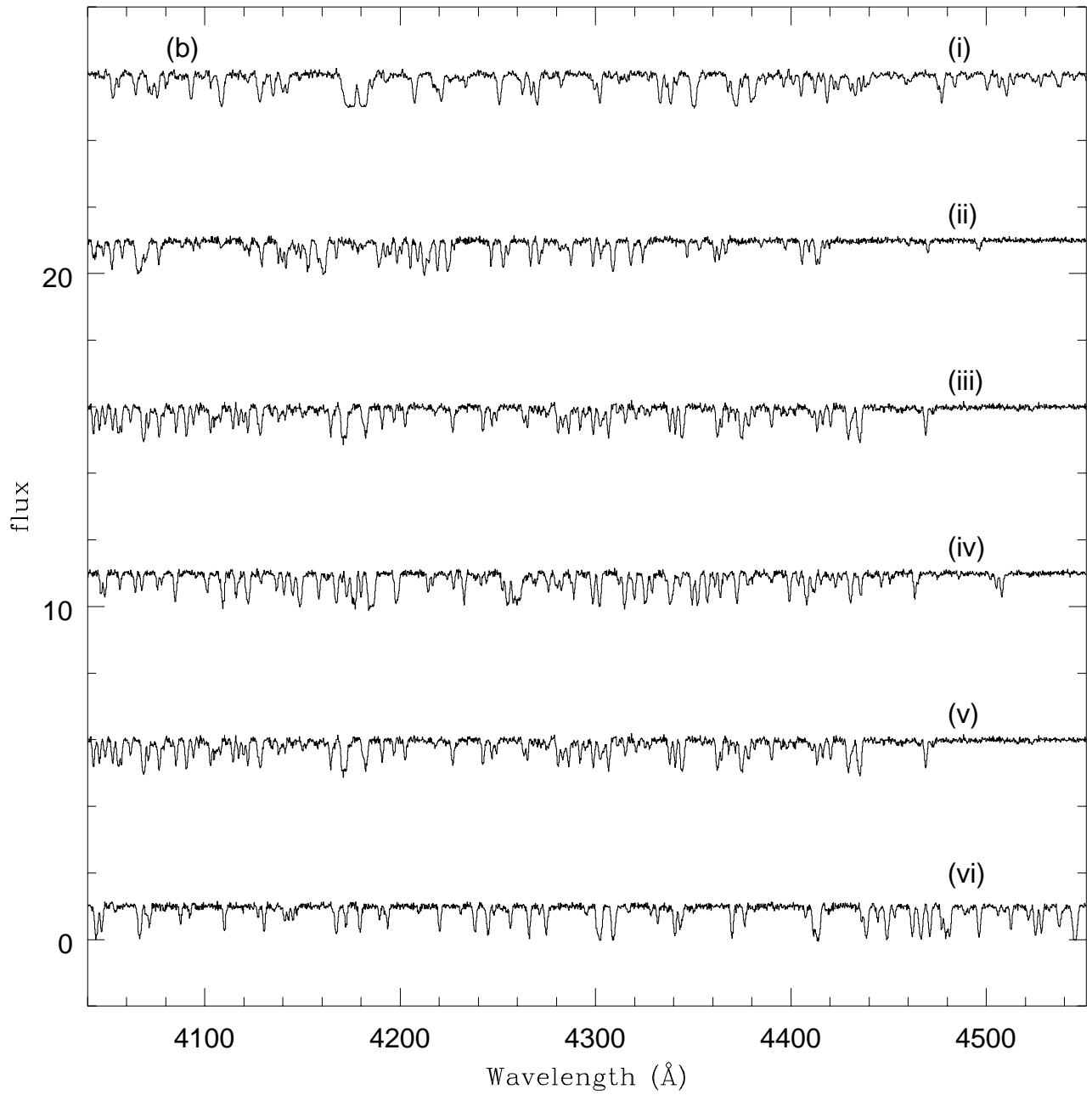


FIG. 10.— Sample simulation spectra plotted with data, flux scale is arbitrary. (a)0014+813: (i)data, (ii)input  $\log[J(\nu_0)]=-23.0$ , (iii)input  $\log[J(\nu_0)]=-22$ , (iv)input  $\log[J(\nu_0)]=-21.3$ , (v)input  $\log[J(\nu_0)]=-20.0$ , (vi)input  $\log[J(\nu_0)]=-19.0$ ; (b)1700+643: (i)-(vi) same as in (a)



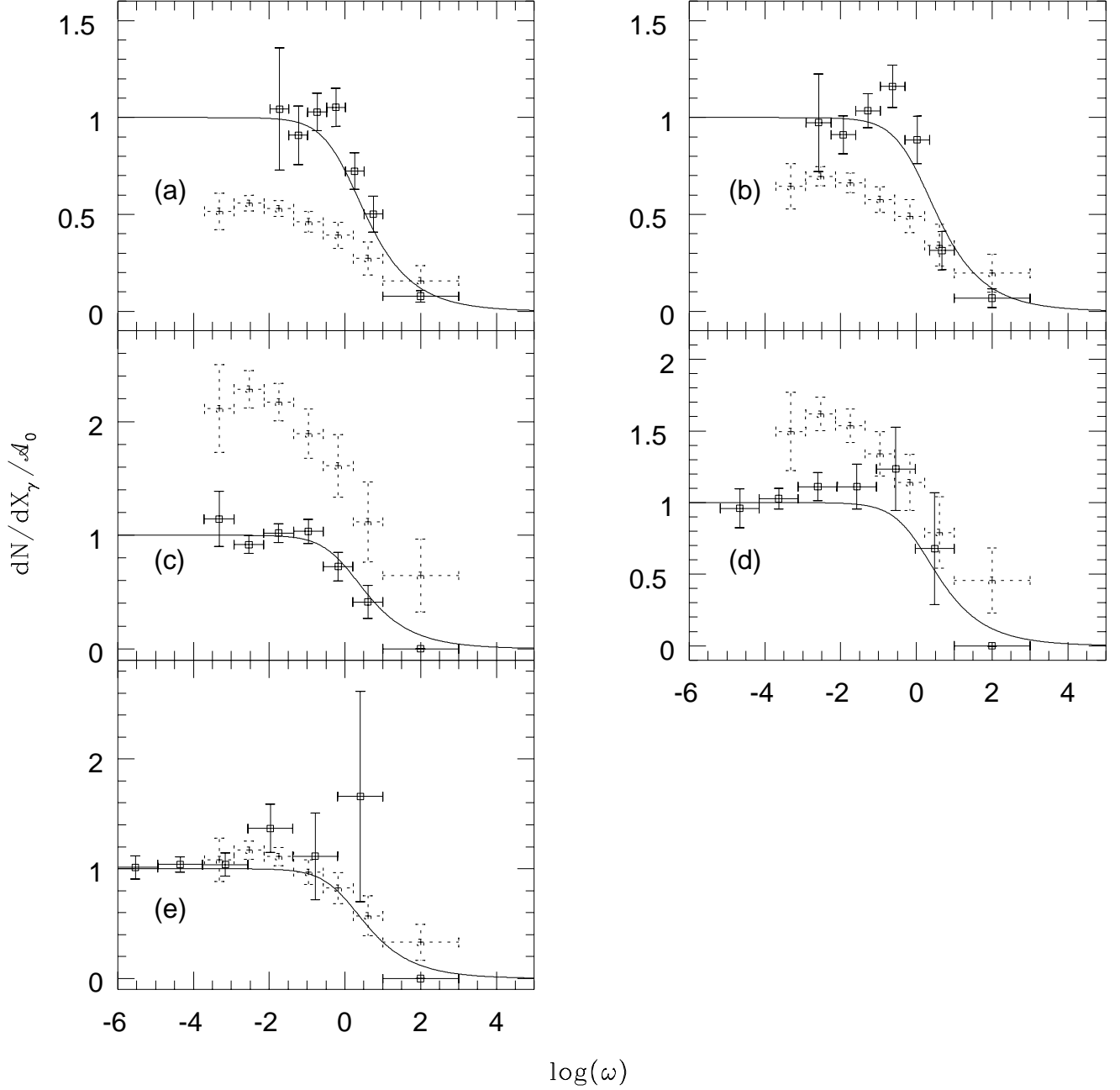


FIG. 11.— Number distribution per coevolving redshift coordinate for the best fit values of  $J(\nu_0)$  listed in Table 7; solid lines- simulation, dotted lines- data, scaled by the relevant value of  $A_0$  in Table 7: (a)input  $\log[J(\nu_0)]=-23.0$ ; (b)input  $\log[J(\nu_0)]=-22$ ; (c)input  $\log[J(\nu_0)]=-21.3$ ; (d)input  $\log[J(\nu_0)]=-20.0$ ; (e)input  $\log[J(\nu_0)]=-19.0$

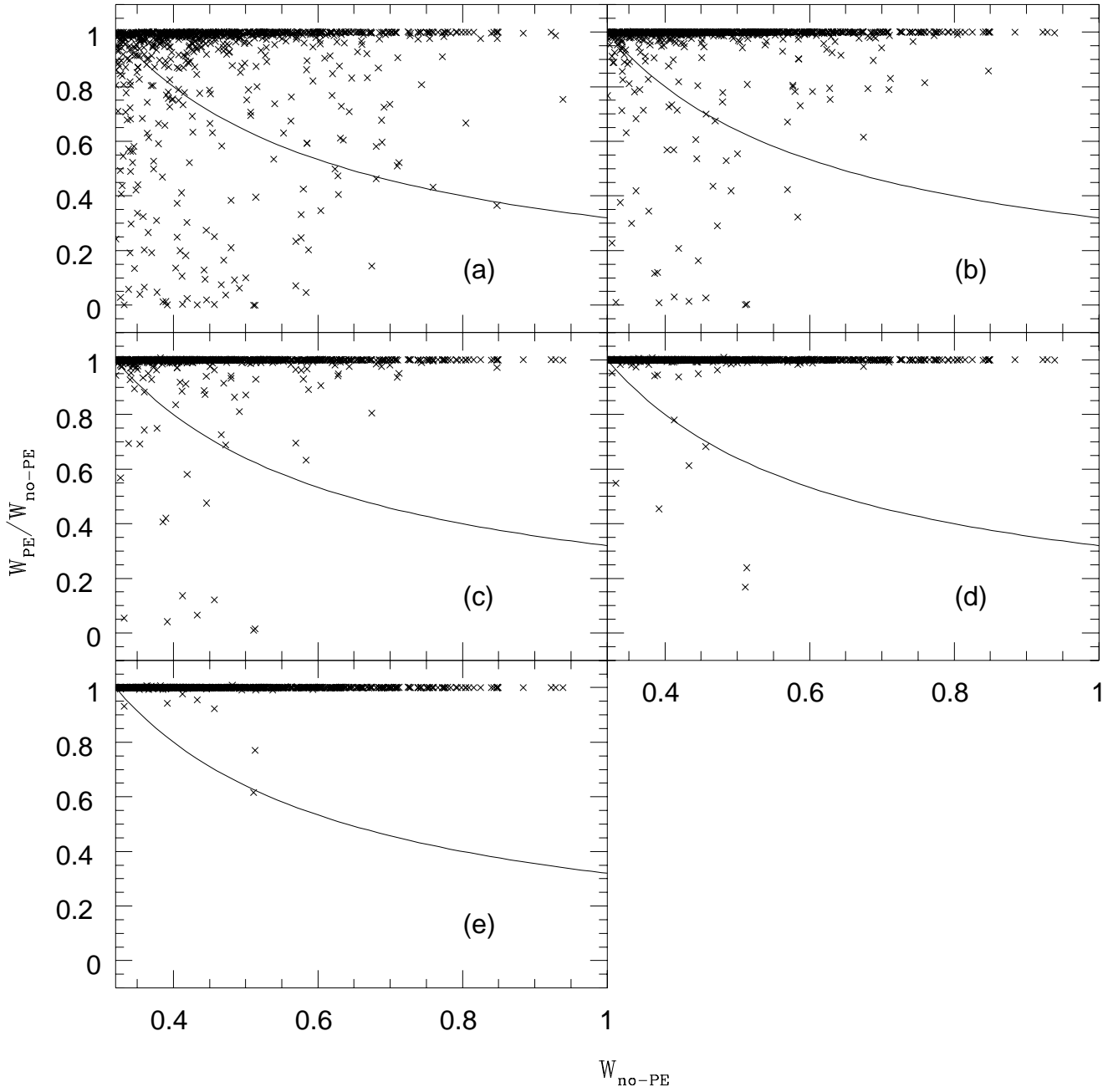


FIG. 12.— Curve of growth effects: ratio of proximity effect to nonproximity effect rest equivalent width for all lines versus nonproximity effect rest equivalent width; solid line represents the detection threshold  $W_{PE} = 0.32 \text{ \AA}$ ; (a)-(e) as in Fig. 11



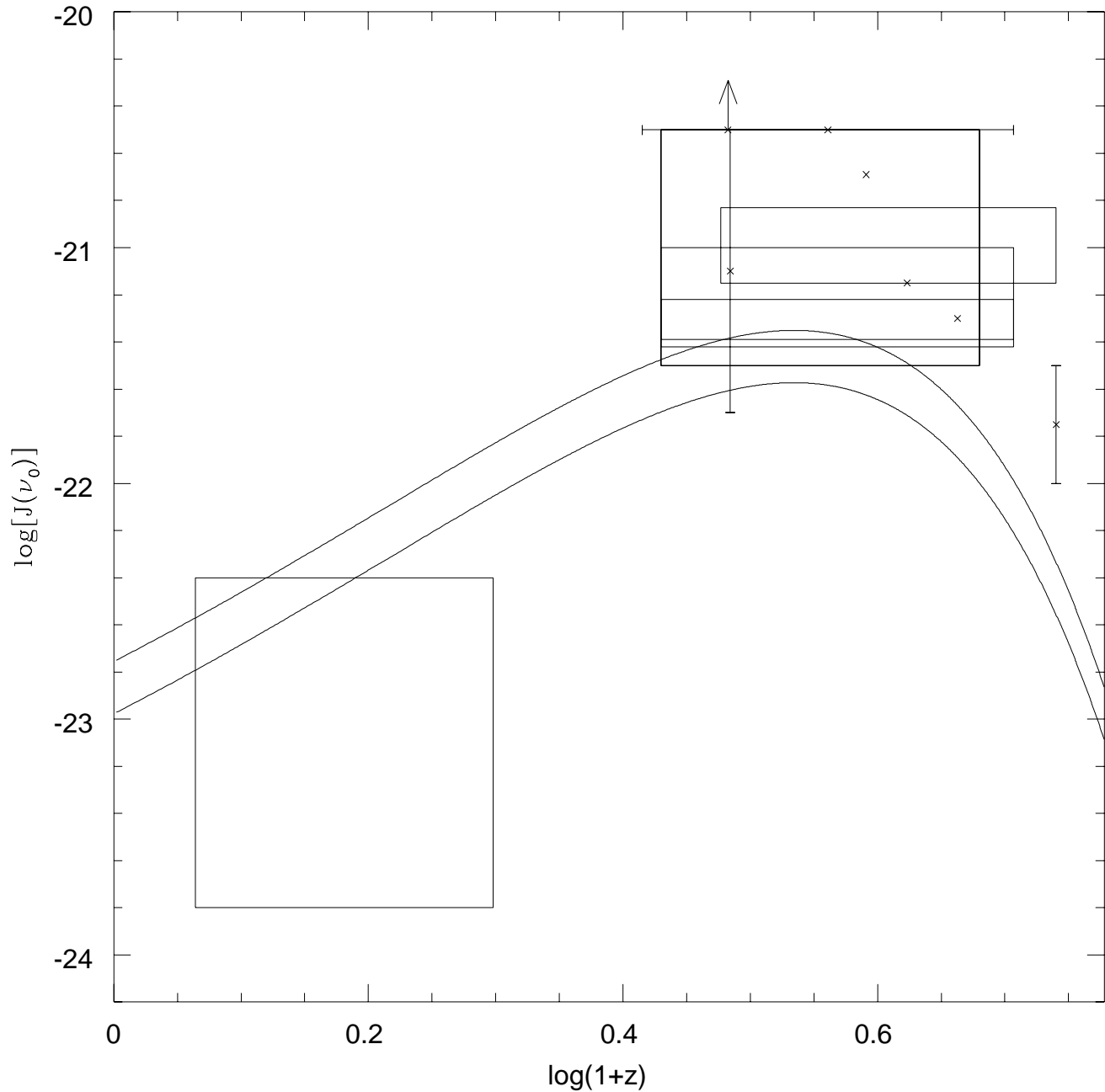


FIG. 13.— Measurements of  $\log[J(\nu_0)]$  vs. redshift: points and error bars are taken from Table 8. The upper limit set by Bunker et al. (1998) at  $z \sim 3$  is included. Measurements over extended redshift ranges and the errors in those measurements are indicated by boxes. The solid curves are derived from the Haardt & Madau (1996) model for the HI photoionization rate as a function of redshift for QSO spectral indices of 0 (lower curve) and 2 (upper curve). Overall, measurements at  $z=2-3$  agree well with one another and with the predictions of the Haardt & Madau (1996) model.

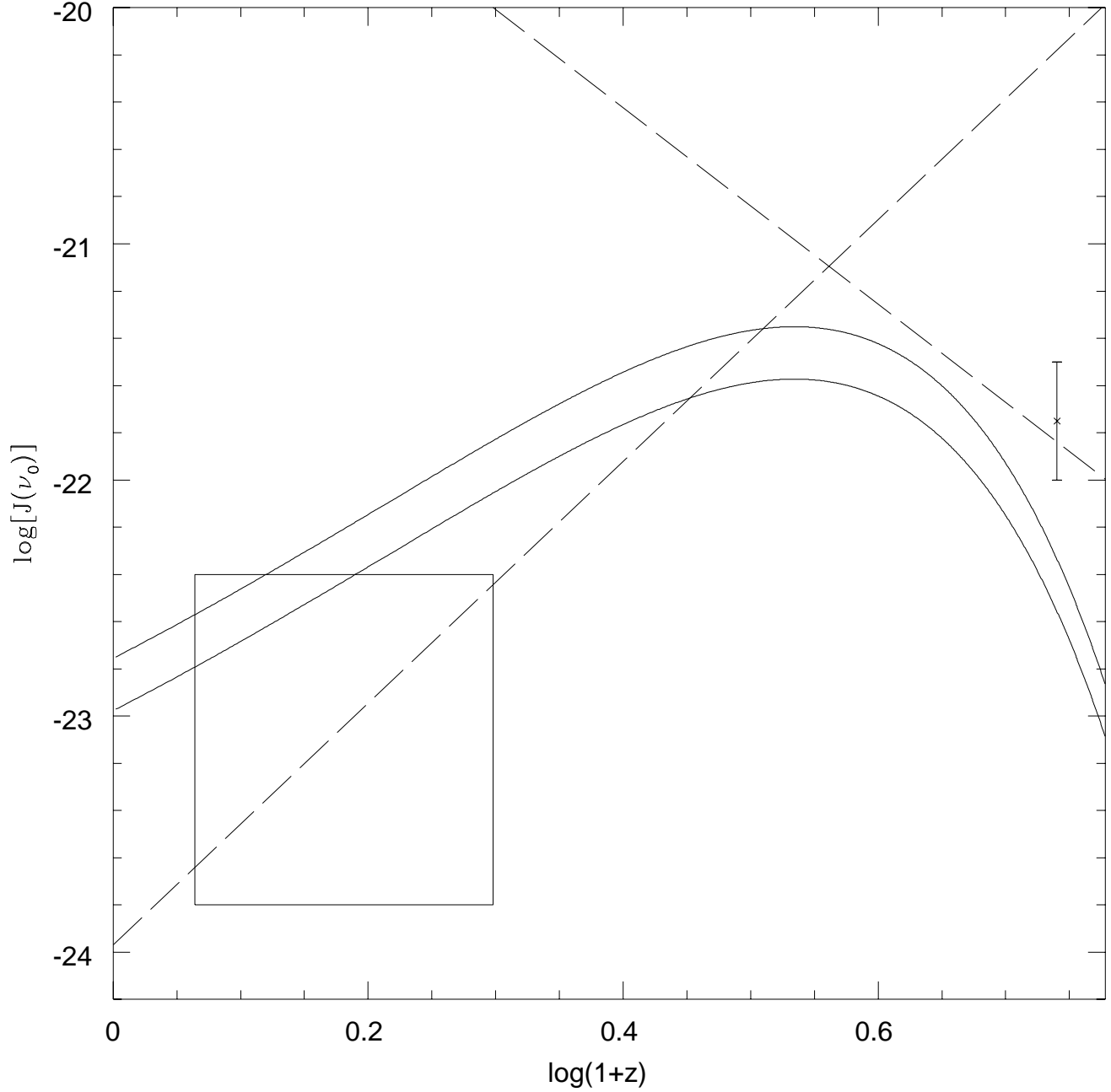


FIG. 14.— Power law fits to  $\log[J(\nu_0)]$  as a function of redshift:  $J(\nu_0, z) = J(\nu_0, 0)(1+z)^j$ . The dashed lines indicate the two lowest  $\chi^2$  fits to the data:  $(j, \log[J(\nu_0, 0)]) = (5.12, -23.97)$  and  $(-4.16, -18.76)$ . The solid curves are the Haardt & Madau (1996) models as shown in Figure 13. The Haardt & Madau (1996) models are turning over at the redshift of the data, precluding a strong constraint on the parameters  $j$  and  $J(\nu_0, 0)$ ; but the lowest  $\chi^2$  fit extends to low redshift to match the Kulkarni & Fall (1993) measurement shown by the box, while the next lowest  $\chi^2$  fit extends to high redshift to match the Williger et al. (1994) measurement, the point at  $z=4.5$ .

TABLE 1  
SPECTROPHOTOMETRY OBSERVATIONS

QSO	Date	Exposure (seconds)	Airmass	Wavelength Coverage (Å)
0006+020	29Nov1994	1800	1.15	3150-6385
0027+018	22Sep1992	1800	1.28	3467-6475
0037-018	29Nov1994	2400	1.27	3150-6385
0049+007	29Nov1994	1800	2.05	3125-6380
0123+257	29Nov1994	1800	1.55	3125-6380
0153+744	29Nov1994	1800	1.38	3125-6380
0348+061	22Sep1992	1800	1.13	3465-6475
1323-107	28Mar1995	1800	1.56	3115-6400
1346-036	28Mar1995	1800	1.27	3115-6400
1422+231	22Apr1996	1800	1.31	5235-7554
1603+383 <sup>a</sup>	04July1995	450	1.03	3663-7544
2134+004	22Sep1992	1800	1.29	3465-6483
2251+244	29Nov1994	1800	1.01	3150-6385
2254+022	22Sep1992	1800	1.18	3470-6480

Instrument Set-up for 1422+231: SO B&C, 600 l mm<sup>-1</sup> 1<sup>st</sup> order,  $\lambda_b=6681$  Å, 1.5'' slit; for 1603+383: FLWO FAST, 300 l mm<sup>-1</sup> 1<sup>st</sup> order,  $\lambda_b=4750$ , 3'' slit

<sup>a</sup>spectrum donated by Hamburg/CfA Bright Quasar Survey in advance of publication

TABLE 2  
SUMMARY OF NARROW EMISSION LINE OBSERVATIONS

Name	V	Instrument	Date	Exposure (sec.)	Wavelength Coverage (μm)
0000-263	17.5	OSIRIS	27Jul1994	4800	1.20 - 1.46
0014+813	16.5	CRSP	07Dec1993	1200	1.18 - 1.26
		FSpec	26Nov1993	5280	1.96 - 2.39
0114-089	17.4	CRSP	04Dec1993	3180	1.10 - 1.35
0636+680	19.0	CRSP	04Dec1993	4800	1.09 - 1.35
		CRSP	05Dec1993	2820	1.96 - 2.10
0836+710	16.5	B&C	29Mar1995	1800	0.52 - 0.96
0956+122	17.5	CRSP	04Dec1993	8220	1.10 - 1.35
		FSpec	27Nov1993	5280	1.96 - 2.38
1159+124	17.5	CRSP	05Dec1993	3180	1.09 - 1.35
		FSpec	29Nov1993	4320	1.97 - 2.38
1207+399	17.5	FSpec	21May1994	600	1.98 - 2.41
1208+101	17.5	CRSP	06Dec1993	4800	2.00 - 2.42
1408+009	18.0	FSpec	02Apr1996	3840	1.46 - 1.73
			02Apr1996	1920	1.99 - 2.40
1422+231	16.5	FSpec	21May1994	1920	1.98 - 2.41
1435+638	15.0	FSpec	02Apr1996	1920	1.99 - 2.40
2126-158	17.3	CRSP	05Dec1993	3180	1.08 - 1.35
		OSIRIS	24Sep1994	7680	1.96 - 2.35

TABLE 3  
SPECTROPHOTOMETRIC PROPERTIES

QSO (a)	$N_{HI}$ ( $10^{20}$ cm $^{-2}$ ) (b)	$f_{\nu}^{obs}$ (912 Å) (c)	$\alpha$ (d)	$f_{\nu}^{obs}$ (e)	$f_{\nu}$ (912 Å) (f)	Ref. (g)
0006+020*	3.02		0.26	354 (1450 Å)	313	1
0027+014	2.93		-0.38	219 (1450 Å)	183	1
0037-018	2.81		-0.27	45 (1450 Å)	51	1
0049+007	2.67		0.31	324 (1450 Å)	280	1
0123+257*	6.88		1.12	237 (1450 Å)	141	1
0150-202*	1.29			529 (1430 Å)	430	2,3
0153+744*	22.74		0.18	1023 (1450 Å)	940	1
0226-038	2.35			582 (1800 Å)	425	4
0348+061	12.33		0.12	513 (1450 Å)	485	1
0400+258	7.82		1.54		199	5
0747+610	4.77			500 (1800 Å)	365	4
0819-032	6.16		0.33	63 (1450 Å)	54	6
0836+710*	2.93				652	
0848+155	3.14		0.07	198 (1450 Å)	191	7,8
0936+368	1.36				386	
0952+335	1.37				370	
0955+472*	1.04				188	
0956+122	3.10	140	0.49	448 (1450 Å)	356	9
1009+299	2.30				1217	
1207+399	2.10		0.59	319 (1450 Å)	242	1,8
1210+175*	2.67				285	
1231+294	1.54				980	
1323-107	2.64		-0.30	303 (1450 Å)	349	1
1329+412*	0.99		0.33		750	10
1337+285*	1.17				339	
1346-036	2.51		0.091	458 (1450 Å)	439	1
1358+115*	1.81		1.10	345 (1450 Å)	207	6
1406+492	1.77				392	
1408+009	3.04		0.91	99 (1450 Å)	64	1
1421+330	1.23	58	0.54	914 (1450 Å)	711	11,7
1422+231*	2.52		-1.21	211 (1450 Å)	371	1
1435+638	1.68	55		1244 (1800 Å)	909	12,4
1603+383*	1.32		0.36	550 (1450 Å)	464	1,13
1604+290	3.24				428	
1715+535	2.69	36	1.26	875 (1800 Å)	371	11,10,4
2134+004	4.03		0.04	35 (1450 Å)	34	1,14
2251+244*	5.18		1.53	243 (1450 Å)	119	1
2254+024	5.32		0.20	116 (1450 Å)	106	1
2310+385	10.62				419	
2320+079	5.04				306	
2329-020	4.45				451	

<sup>a</sup>QSO name; an asterisk denotes a metal line system within 5000 km s $^{-1}$  of the QSO emission redshift; in the case of 1422+231, the QSO is a known lens

<sup>b</sup>Galactic  $N_{HI}$  in units of  $10^{20}$  cm $^{-2}$  from program COLDEN using Stark et al. (1992)

<sup>c</sup>Observed flux in  $\mu$ Jy at the Lyman limit from reference in (g)

<sup>d</sup>Observed spectral index between Ly $\alpha$  and C IV emission lines or in the vicinity of the flux listed in (e) from reference in (g); in general, values are based upon spectra corrected for Galactic reddening if  $E(B-V) \gtrsim 0.03$

<sup>e</sup>Observed flux in  $\mu$ Jy at the rest wavelength indicated in parentheses from reference in (g)

<sup>f</sup>Extrapolated Lyman limit flux in  $\mu$ Jy from measured flux in (e), when available, or V magnitude given in Table 1 of Paper I.; if no observed spectral index available, value of 0.46 used (Francis 1996)

<sup>g</sup>REFERENCES: (1) this paper; (2) MacAlpine & Feldman 1982; (3) Griffith et al. 1994; (4) Steidel & Sargent 1991; (5) Cheng, Gaskell, & Koratkar 1991; (6) Pei, Fall & Bechtold 1991; (7) Uomoto 1984; (8) Barthel et al. 1988; (9) Sargent, Steidel, & Boksenberg 1989; (10) Baldwin, Wampler, & Gaskell 1989; (11) Koratkar, Kinney, & Bohlin 1992; (12) Lanzetta, Turnshek & Sandoval 1993 (13) Hamburg/CfA Bright Quasar Survey (unpublished); (14) Perez, Penston, & Moles 1989

TABLE 4  
MEASUREMENTS OF  $J(\nu_0)$

Sample (a)	$\mathcal{N}_{lines}$ (b)	$\gamma, \text{norm.}$ (c)	method (d)	$\log[(J(\nu_0))]$ (e)	$\chi^2$ (f)	$\mathcal{N}_{points}$ (g)	$Q_{\chi^2}$ (h)	Figure (i)
1	518	1.9260,5.8882	BDO	$-21.40^{+1.1}_{-0.69}$	3.05	7	0.88	6(a)
1	518	1.9260,3.9709	ML	$-21.58^{+0.30}_{-0.23}$	20.3	6	0.0024	8(a)
2	1286	1.6749,7.5723	BDO	$-20.90^{+0.61}_{-0.48}$	5.22	7	0.63	6(b)
2	1286	1.6749,4.6637	ML	$-20.83^{+0.23}_{-0.20}$	6.32	6	0.38	8(b)
3	1286	1.6749,7.5723	BDO	$-21.00^{+0.57}_{-0.36}$	7.19	7	0.40	6(c)
3	1286	1.6749,4.6709	ML	$-20.83^{+0.24}_{-0.22}$	7.41	6	0.28	8(c)
4	1286	1.6749,7.5723	BDO	$-21.15^{+0.17}_{-0.43}$	6.54	7	0.47	6(d)
4	1286	1.6749,4.6617	ML	$-21.17^{+0.19}_{-0.15}$	3.53	6	0.73	8(d)
5	763	-0.2848,110.13	BDO	$-20.75^{+0.16}_{-0.86}$	3.31	7	0.85	6(e)
5	763	-0.2848,69.934	ML	$-21.18^{+0.19}_{-0.21}$	4.92	5	0.42	8(e)
6	523	1.3754,10.240	BDO	$-21.15^{+0.11}_{-0.92}$	3.97	7	0.78	6(f)
6	523	1.3754,7.4759	ML	$-21.46^{+0.34}_{-0.29}$	15.5	6	0.016	8(f)
7	261	2.3284,2.6809	BDO	$-21.45^{+0.40}_{-0.53}$	3.03	7	0.88	6(j)
8	666	1.5361,9.1237	BDO	$-21.25^{+0.28}_{-0.45}$	4.32	7	0.74	6(g)
9	620	2.0242,4.6980	BDO	$-21.05^{+0.20}_{-0.42}$	3.49	7	0.83	6(h)
10	671	0.5468,24.655	BDO	$-20.45^{+0.37}_{-0.90}$	3.05	7	0.88	6(i)

<sup>a</sup>(1) DB96 sample; (2) all lines, Ly $\alpha$  QSO redshifts; (3) all lines, using narrow line redshifts where available, Ly $\alpha$  redshifts otherwise; (4) all lines, narrow line redshifts where available, Ly $\alpha$  redshifts + 400 km s<sup>-1</sup> otherwise; (5) high z lines, QSO redshifts as in case (4) ; (6) low z lines, QSO redshifts as in case (4); (7) lines from QSOs with damped Ly $\alpha$  systems only, QSO redshifts as in case (4); (8) high luminosity QSOs, QSO redshifts as in case (4); (9) low luminosity QSOs, QSO redshifts as in case (4); (10) weak lines only:  $0.16\text{\AA} < W < 0.32\text{\AA}$ , QSO redshifts as in case (4)

<sup>b</sup>number of Ly $\alpha$  forest lines in sample

<sup>c</sup>Equ. 1 parameters  $\gamma$  and  $\mathcal{A}_0$  from maximum likelihood fit to data; when the method listed is ML, the normalization listed is equal to  $\mathcal{A}_0(N_{lim}/N_0)^{\beta-1}(\beta-1)^{-1}$  (see text, Paper I)

<sup>d</sup>BDO- Bajtlik, Duncan, & Ostriker (1988), ML- maximum likelihood, see Kulkarni & Fall (1993)

<sup>e</sup>Best fit value of  $\log[(J(\nu_0))]$  in units of ergs s<sup>-1</sup> cm<sup>-2</sup> Hz<sup>-1</sup> sr<sup>-1</sup>

<sup>f</sup> $\chi^2$  of data vs. the ionization model used

<sup>g</sup>number of points used to calculate  $\chi^2$

<sup>h</sup> $\chi^2$  probability for the ionization model used

<sup>i</sup>Figure displaying number distribution per coevolving redshift interval,  $d\mathcal{N}/dX_\gamma$

TABLE 5  
EMISSION LINE REDSHIFTS FOR QSOs INCLUDED IN MEASUREMENT OF  
 $J(\nu_0)^a$

QSO	z	line <sup>b</sup>	Ref. <sup>c</sup>
0000-263*	4.111	Ly $\alpha$	1
	4.116	Mg II	2
0001+087	3.243	Ly $\alpha$	3
0002+051	1.899	Ly $\alpha$	4
	1.899	Mg II	5
0002-422	2.763	Ly $\alpha$	6
0006+020*	2.340	Ly $\alpha$	2
0014+813	3.386	Ly $\alpha$	1
	3.379	Mg II	2
	3.404	H $\beta$	2
0027+014	2.333	Ly $\alpha$	2
	2.310	H $\beta$	7
0029+073	3.261	Ly $\alpha$	1
0037-018	2.341	Ly $\alpha$	2
0049+007	2.275	Ly $\alpha$	2
	2.279	[OIII] $\lambda$ 5007	8
0058+019	1.959	Ly $\alpha$	9
	1.964	Mg II	5
0100+130	2.690	Ly $\alpha$	6
0114-089	3.194	Ly $\alpha$	9
	3.192	Mg II	2
0119-046*	1.951	Ly $\alpha$	1
	1.964	Mg II	5
0123+257*	2.358	Ly $\alpha$	10
	2.370	[OIII] $\lambda\lambda$ 4959,5007	8
0142-100*	2.727	Ly $\alpha$	9
0150-202*	2.148	Ly $\alpha$	2
	2.149	Mg II	5
0153+744*	2.340	Ly $\alpha$	2
	2.341	[OIII] $\lambda$ 5007	8
0226-038	2.067	Ly $\alpha$	2
	2.073	Mg II	5
	2.073	[OIII] $\lambda\lambda$ 4959,5007	8
0237-233	2.224	Ly $\alpha$	9
	2.200	[OIII] $\lambda$ 5007	7
0256-000	3.374	Ly $\alpha$	1
0301-005	3.228	Ly $\alpha$	1
0302-003*	3.286	Ly $\alpha$	1
0334-204	3.131	Ly $\alpha$	1
0348+061	2.057	Ly $\alpha$	2
	2.056	Mg II	5
0400+258	2.108	Ly $\alpha$	2
0421+019	2.050	Ly $\alpha$	4
	2.056	Mg II	5
0424-131*	2.165	Ly $\alpha$	11
	2.166	Mg II	5
	2.163	H $\alpha$	12
0453-423	2.656	Ly $\alpha$	6
0636+680	3.167	Ly $\alpha$	1
	3.184	Mg II	2
	3.187	H $\beta$	2
0731+653	3.033	Ly $\alpha$	1
0747+610	2.491	Ly $\alpha$	2
0831+128	2.739	Ly $\alpha$	3
0836+710*	2.189	Ly $\alpha$	2
	2.197	Mg II	2

TABLE 5—*Continued*

QSO	z	line <sup>b</sup>	Ref. <sup>c</sup>
	2.218	[OIII] $\lambda$ 5007	8
0837+109	3.323	Ly $\alpha$	9
0848+155	2.019	Ly $\alpha$	2
	2.014	Mg II	5
0848+163*	1.925	Ly $\alpha$	13
	1.922	Mg II	5
0905+151	3.173	Ly $\alpha$	3
0913+072	2.785	Ly $\alpha$	9
0936+368	2.025	Ly $\alpha$	2
0938+119	3.192	Ly $\alpha$	3
0952+335	2.504	Ly $\alpha$	2
0955+472	2.482	Ly $\alpha$	2
0956+122	3.033	Ly $\alpha$	2
	3.299	Mg II	2
	3.314	H $\beta$	2
	3.308	[OIII] $\lambda$ 5007	2
1009+299	2.633	Ly $\alpha$	2
1017+280	1.928	Ly $\alpha$	9
1033+137	3.092	Ly $\alpha$	3
1115+080*	1.727	Ly $\alpha$	14
1159+124*	3.505	Ly $\alpha$	9
	3.508	Mg II	2
	3.497	H $\beta$	2
	3.497	[OIII] $\lambda$ 5007	2
1206+119	3.108	Ly $\alpha$	3
1207+399	2.451	Ly $\alpha$	2
	2.463	H $\alpha$	2
1208+101*	3.822	Ly $\alpha$	3
	3.833	H $\beta$	2
	3.802	[OIII] $\lambda$ 5007	2
1210+175*	2.564	Ly $\alpha$	2
1215+333	2.606	Ly $\alpha$	14
1225-017	2.831	Ly $\alpha$	15
1225+317	2.200	Ly $\alpha$	6
	2.226	[OIII] $\lambda$ 5007	8**
1231+294	2.018	Ly $\alpha$	2
1247+267	2.041	Ly $\alpha$	9
1315+472	2.590	Ly $\alpha$	3
1323-107	2.360	Ly $\alpha$ /C IV	16
1329+412*	1.934	Ly $\alpha$	2
1334-005	2.842	Ly $\beta$	3
1337+285*	2.541	Ly $\alpha$	2
1346-036	2.356	Ly $\alpha$	2
	2.368	Mg II	12
	2.362	[OIII] $\lambda$ 5007	8
	2.367	H $\alpha$	12
1358+115*	2.589	Ly $\alpha$	2
1400+114	3.177	Ly $\alpha$	3
1402+044	3.208	Ly $\alpha$	17
1406+492	2.161	Ly $\alpha$	2
1408+009	2.262	Ly $\alpha$	2
	2.260	[OIII] $\lambda$ 5007	2
	2.265	H $\alpha$	2
1410+096	3.313	Ly $\alpha$	3
1421+330	1.903	Ly $\alpha$	2
	1.906	Mg II	5

TABLE 5—*Continued*

QSO	z	line <sup>b</sup>	Ref. <sup>c</sup>
1422+231*	3.624	Ly $\alpha$	2
	3.630	H $\beta$	2
	3.623	[OIII] $\lambda$ 5007	2
1435+638	2.063	Ly $\alpha$	2
	2.061	Mg II	5
	2.066	[OIII] $\lambda\lambda$ 4959,5007	8
	2.065	H $\alpha$	2
1442+101	3.560	Ly $\alpha$	17
1451+123	3.251	Ly $\alpha$	3
1511+091*	2.877	C IV	9
1512+132	3.120	Ly $\alpha$	3
1548+092	2.759	Ly $\alpha$	9
1601+182*	3.227	Ly $\alpha$	3
1602+178*	2.989	Ly $\alpha$	3
1603+383*	2.510	Ly $\alpha$	18
1604+290	1.962	Ly $\alpha$	2
1607+183	3.120	Ly $\alpha$	17
1614+051	3.216	Ly $\alpha$	17
	3.214	[OIII] $\lambda$ 5007	19
1623+269*	2.526	Ly $\alpha$	3
1700+642	2.744	Ly $\alpha$	15
1715+535	1.935	Ly $\alpha$	2
	1.932	Mg II	5
1738+350	3.239	Ly $\alpha$	3
1946+770	3.020	Ly $\alpha$	15
2126-158	3.280	Ly $\alpha$	6
	3.284	Mg II	2
	3.298	H $\beta$	2
	3.292	[OIII] $\lambda$ 5007	2
2134+004	1.941	Ly $\alpha$	2
2233+131	3.301	Ly $\alpha$	1
2233+136	3.207	Ly $\alpha$	1
2251+244*	2.335	Ly $\alpha$	17
	2.359	[OIII] $\lambda$ 5007	8
2254+024	2.089	Ly $\alpha$	2
	2.090	Mg II	5
	2.179	Ly $\alpha$	2
2310+385	2.181	[OIII] $\lambda\lambda$ 4959,5007	8
	3.041	Ly $\alpha$	1
2320+079	2.088	Ly $\alpha$	2
2329-020	1.896	Ly $\alpha$	2

<sup>a</sup>Objects with both [OIII] and Ly $\alpha$ , Mg II, or Balmer redshifts were used to construct histograms in Figure 9; Objects marked with an asterisk are excluded from the proximity effect analysis on the basis of associated absorption or gravitational lensing

<sup>b</sup>Emission lines used to measure redshift.

<sup>c</sup>REFERENCES: (1) Sargent et al. 1989; (2) this paper; (3) B94; (4) Young et al. 1982a; (5) Steidel & Sargent 1991; (6) Sargent et al. 1980; (7) Baker et al. 1994; (8) McIntosh et al. 1999a (\*\*1225+317 measurement quoted as uncertain due to weak [O III] emission and low S/N); (9) Sargent et al. 1988; (10) Schmidt & Olsen 1968; (11) Burbidge 1970; (12) Espey et al. 1989; (13) Young et al. 1982b; (14) Wills & Wills 1979; (15) DB96; (16) Kunth et al. 1981; (17) Barthel et al. 1990; (18) Hamburg/CfA Bright Quasar Survey (unpublished); (19) Bremer & Johnstone 1995



TABLE 6  
IONIZATION RATES

$A, B, z_c, S$	Ref. (a)	$\chi^2$ (b)	$Q_{\chi^2}$ (c)
$6.7\text{e-}13 \text{ s}^{-1}, 0.43, 2.30, 1.95$	1	11.2	0.12
$5.6\text{e-}13 \text{ s}^{-1}, 0.60, 2.22, 1.90$	2	11.8	0.10
$1.2\text{e-}12 \text{ s}^{-1}, 0.58, 2.77, 2.38$	2	7.15	0.41

<sup>a</sup>(1)Haardt & Madau (1996); (2)Fardal et al. (1998)

<sup>b</sup> $\chi^2$  of data vs. the BDO ionization model

<sup>c</sup> $\chi^2$  probability for the BDO ionization model

TABLE 7  
SIMULATION RESULTS

Input $\log[(J(\nu_0))]$ (a)	$\gamma, \mathcal{A}_0$ (b)	$\log[(J(\nu_0))]$ recovered (c)	$\chi^2$ (d)	$Q_{\chi^2}$ (e)
-23.0	1.5722, 11.043	$-22.75^{+0.28}_{-0.19}$	11.2	0.12
-22.0	1.6869, 8.8367	$-21.80^{+0.40}_{-0.28}$	11.3	0.12
-21.3	2.6267, 2.6960	$-21.00^{+0.28}_{-0.60}$	2.68	0.91
-20.0	2.2511, 3.8084	$-19.50^{+1.86}_{-0.84}$	3.90	0.79
-19.0	2.0302, 5.2704	$-18.50^{+0.66}_{-1.56}$	5.28	0.62

<sup>a</sup>value of  $\log[(J(\nu_0))]$  used for modifying absorber column densities according to Equations 7 and 10

<sup>b</sup>Equ. 1 parameters  $\gamma$  and  $\mathcal{A}_0$  from maximum likelihood fit to data

<sup>c</sup>value of  $\log[(J(\nu_0))]$  from simulated spectra using the standard BDO technique

<sup>d</sup> $\chi^2$  of data vs. the BDO ionization model

<sup>e</sup> $\chi^2$  probability for the BDO ionization model

TABLE 8  
LITERATURE PROXIMITY EFFECT MEASUREMENTS OF  $J(\nu_0)$

$\log[(J(\nu_0))]$	$z$	$\mathcal{N}_{QSOs}$	Ref. <sup>a</sup>
$-23.2^{+0.8}_{-0.6}$	0.16-0.99	13	1
$-20.5^{+\infty}_{-1.3}$	1.8-2.3	3	2 <sup>b</sup>
$-21.1 \pm 0.6$	2.0	1	2
-21.15	3.2	1	3
-21.3	3.6	1	4
$-21.0 \pm 0.5$	1.7-3.8	38	5
$-21.0 \pm 0.5$	1.7-3.8	19	6
-20.5	1.6-4.1	49	7
$-21.3^{+0.08}_{-0.09}$	1.7-4.1	10	8
$-21.1^{+0.15}_{-0.27}$	1.7-4.1	74	9
$-21.0^{+0.17}_{-0.15}$	2.0-4.5	11	10
-22.0 - -21.5	4.5	1	11

<sup>a</sup> (1) Kulkarni & Fall 1993; (2) Fernández-Soto et al. 1995; (3) Giallongo et al. 1993; (4) Cristiani et al. 1995; (5) BDO; (6) LWT; (7) B94; (8) Giallongo et al. 1996; (9) this paper; (10) Cooke et al. 1997; (11) Williger et al. (1994)

<sup>b</sup> measured from the proximity effect to due a foreground QSO; not able to set an upper limit